

The effect of collisional enhancement of Balmer lines on the determination of the primordial helium abundance

V. Luridiana¹

Instituto de Astrofísica de Andalucía (CSIC), Granada, Spain

A. Peimbert² and M. Peimbert²

Instituto de Astronomía (UNAM), México D.F., Mexico

and

M. Cerviño^{1,3}

Instituto de Astrofísica de Andalucía (CSIC), Granada, Spain

Laboratorio de Astrofísica Espacial y Física Fundamental (INTA), Madrid, Spain

vale@iaa.es, antonio@astroscu.unam.mx, peimbert@astroscu.unam.mx,
mcs@laeff.esa.es

ABSTRACT

This paper describes a new determination of the primordial helium abundance (Y_P), based on the abundance analysis of five metal-poor extragalactic H II regions. For three regions of the sample (SBS 0335–052, I Zw 18, and H 29) we present tailored photoionization models based on improved calculations with respect to previous models. In particular, we use the photoionization models to study quantitatively the effect of collisional excitation of Balmer lines on the determination of the helium abundance (Y) in the individual regions. This effect is twofold: first, the intensities of the Balmer lines are enhanced with respect to the pure recombination value, mimicking a higher hydrogen abundance; second, the observed reddening is larger than the true extinction, due to the differential effect of collisions on different Balmer lines. In addition to these effects, our analysis takes into account the following features of H II regions: (i) the temperature structure, (ii) the density structure, (iii) the presence of neutral helium, (iv) the collisional excitation of the He I lines, (v) the underlying absorption of the He I lines, and (vi) the optical thickness of the He I lines. The object that shows the highest increase in Y after the inclusion of collisional effects in the analysis is SBS 0335–052, whose helium abundance has been revised by $\Delta Y = +0.0107$. The revised Y values for the five objects in our sample yield an increase of $+0.0035$ in Y_P , giving $Y_P = 0.2391 \pm 0.0020$.

Subject headings: galaxies: abundances — galaxies: individual (SBS 0335–052, I Zw 18, H 29) — galaxies: ISM — H II regions — ISM: abundances

1. Introduction

In this work we describe a new determination of the primordial ${}^4\text{He}$ abundance (Y_P), based on the abundance analysis of five metal-poor extragalactic H II regions. The value of Y_P is still one of the missing pieces in the cosmological scenario. According to the standard model of Big-Bang nucleosynthesis, the primordial abundance of four light isotopes (D, ${}^7\text{Li}$, ${}^3\text{He}$, and ${}^4\text{He}$) depends on one parameter only, the baryon-to-photon ratio. Therefore, the four abundance values provide altogether a strong constraint on the cosmological models. Unfortunately, their determination is not an easy task, and each of the four isotopes poses a different challenge. In particular, although ${}^4\text{He}$ is the most abundant of the four and the easiest to measure, it is also the less sensitive to the baryon-to-photon fraction: this feature implies that Y_P determinations must be both accurate to be truthful, and precise to be meaningful. Current Y_P determinations are thought to be accurate to the third decimal digit, a level at which differences still matter from the point of view of cosmology. To improve further, one must take into account all the sources of uncertainty that affect, down to this level, both the accuracy and the precision of Y_P determinations. In the following, we will briefly discuss some of these sources; see also the reviews by Luridiana (2003) and Peimbert et al. (2003) for a more complete discussion of this topic and a quantitative estimate of the error budget in the determination of Y_P .

According to the standard scenario, the universe was born with zero metallicity (Z); hence, Y_P can be determined extrapolating to $Z = 0$ the relationship between Z and the ${}^4\text{He}$ abundance (Y) for a sample of objects. This procedure relies on the determination of the individual Y and Z values, and of the slope dY/dZ of the Y vs. Z curve, which is assumed linear. The uncertainty affecting Y_P depends directly on the uncertainties affecting either of these basic ingredients, i.e. dY/dZ and the ensemble of the (Y, Z) pairs. For this reason, it has long been thought that the best results are obtained from the analysis of extremely low-metallicity objects, such as dwarf irregulars (dIrrs) and blue compact dwarf galaxies (BCDs), since the use of these objects minimizes the uncertainty associated to dY/dZ . However, Peimbert (2003) and Peimbert et al. (2003) have noted that this advantage is outweighed by the relatively higher uncertainty on the Y values, which derives from the (unknown) collisional contribution to the Balmer line intensities: an uncertainty especially affecting these objects since collisional contribution is quite important at high temperatures, and rapidly fades away at intermediate and low temperatures. As we will see throughout the paper, a

precise estimate of this contribution is rather difficult to obtain, and the resulting uncertainty more than offsets the smaller uncertainty in the extrapolation to $Z = 0$. Peimbert (2003) suggests to use moderately low-metallicity regions in the determination of Y_P , because in those regions the collisional contribution can be neglected, and the effect of the uncertainty on the slope is still moderate.

This paper is concerned mainly with the estimation of the collisional contribution to the Balmer lines in low-metallicity regions, and of both the correction and the additional uncertainty it introduces in the value of Y_P . In a previous paper (Peimbert, Peimbert, & Luridiana 2002, hereinafter Paper I) we discussed the effect of temperature structure on the determination of Y_P , and derived a new value of Y_P based on a sample of five extragalactic H II regions with low and very low metallicities: NGC 346, NGC 2363, H 29, SBS 0335–052, and I Zw 18; Paper I also contains a preliminary discussion of the effect of collisions on the determination of Y_P . The abundance analysis of these objects is based on the combined use of standard empirical relations and tailored photoionization models. In the case of NGC 2363, we used the models described in Luridiana, Peimbert, & Leitherer (1999), while NGC 346 has been modeled by Relaño, Peimbert, & Beckman (2002). The models for the remaining three objects will be described in the present paper.

2. The models

The models presented in this paper are based on improved calculations with respect to those mentioned in Paper I. The main changes introduced are the following: (i) the photoionization code Cloudy 94 (Ferland 2000a,b) was used instead of the older version Cloudy 90 (an exhaustive list of the differences between the two versions can be found at <http://www.pa.uky.edu/~gary/cloudy>); (ii) the geometry of the models was modified to improve the fit with the observed quantities; (iii) the ionizing sources were computed with the population synthesis code described in Cerviño et al. (2002), instead of Starburst99 (Leitherer et al. 1999).

2.1. Ionizing spectra

The synthesis code by Cerviño et al. (2002) allows taking into account the sampling effects in the initial mass function (IMF), which is filled stochastically following a Monte Carlo method. While in very massive stellar populations the IMF can be effectively described by an analytical law, in smaller populations sampling effects can be important, and an

analytical description of the IMF artificially introduces fractional numbers of stars in the high-mass end of the mass spectrum, where the statistics is intrinsically low. As a result, those parts of the spectrum depending strongly on the massive star population may be unrealistically represented by an analytical description. The sense of using Monte Carlo simulations is therefore the search for self-consistency, rather than the goal of reproducing the specific stellar content of these clusters. Stated otherwise, we don't aim at reproducing the observed cluster as it is, since specific information on the stellar content of the regions analyzed is not available; we rather attempt to build a synthesis model that is both physically self-consistent, and capable of reproducing the observational constraints. This conditions are sufficient to build meaningful photoionization models.

All the models described in this work assume a Salpeter IMF in the mass range $2 - 120 M_{\odot}$, and evolutionary tracks with stellar metallicity $Z_* = 0.001$ and the standard mass-loss rates by Schaller et al. (1992); the stellar metallicity is the lowest available value among the stellar libraries included in the synthesis code. As for the stellar atmospheres, the code uses the models by Schaerer & de Koter (1997) at $Z = 0.004$ for main sequence (MS) hot stars, those by Schmutz et al. (1992) for Wolf-Rayet (WR) stars, and those by Kurucz (1991) at $Z = 0.002$ for the remaining stars. As a safety check, we have compared the resulting effective rates of ionizing photons (Cerviño et al. 2003) for H^0 , He^0 , He^+ , O^0 , O^+ , and O^{++} to those obtained with the new version of Starburst99 with the atmosphere models by Smith, Norris, & Crowther (2002) and evolutionary tracks with high mass-loss rates (Meynet et al. 1994). The resulting effective rates of ionizing photons in the two codes for H^0 , He^0 , O^0 , and O^+ coincide to better than 0.15 dex for the age range considered in this work, despite the differences in the evolutionary tracks and the atmosphere models. On the other hand, there are strong differences, amounting to more than 0.9 dex, for the effective ionizing rates of He^+ and O^{++} , which determine the abundances of He^{++} and O^{3+} respectively. Hence, our results are virtually independent on the model atmospheres and evolutionary tracks assumed, except for the case of He^{++} (which will be not be used as a constraint: see Section 2.4 below), and the case of O^{3+} , which is an unimportant ion.

The spectra used in the modeling were computed using the following procedure: (i) from the emission rate of ionizing photons $Q(H^0)$ inferred from the observations, and through a comparison with the results of a completely sampled IMF, we have obtained a first estimate of the mass transformed into stars and of the number of stars for the given IMF and mass limits; (ii) from the observed features of the spectrum, we have constrained the age range of each object; for example, the presence of WR features implies that the age of the starburst is in the range $2.9 - 3.1$ Myr for the case of an instantaneous burst (IB), or larger than 2.9 Myr for the case of a continuous star formation (CSF) burst; (iii) with the input parameters obtained in the previous steps, we have performed a large number of Monte Carlo simulations;

(iv) among all the simulations, we have selected those with a $Q(\text{H}^0)$ value consistent with the observations; (v) for those H II regions whose spectra show WR features we have further selected the simulations including WR stars; (vi) finally, we have chosen the simulations with the largest value of the ratio $Q(\text{O}^+)/Q(\text{H}^0)$, where $Q(\text{O}^+)$ is the emission rate of photons with energy $E > 2.6$ Ryd; this choice is motivated by the general tendency in most of our trial models of emitting globally too low oxygen lines: this criterion is a simple way of overcoming this difficulty, since a harder spectra increases the R_{23} parameter (Pagel et al. 1979). The particular features of each object will be discussed in the corresponding section.

2.2. Geometry

This section describes the geometric assumptions made in our models. One of the most important features of H II regions affecting the geometric assumptions made in the modeling is photon leak: for example, Zurita, Rozas, & Beckman (2001) estimate that 25 to 60 percent of the ionizing photons escape from giant H II regions. In a spherically symmetric model, the escape of photons can be modeled in two basic ways, which correspond to two different geometrical scenarios. The first assumes that the actual radius is smaller than the Strömgen radius (R_S), or, equivalently, that the gas cloud ends before it succeeds in absorbing all the ionizing photons. A model with this feature is *density bounded* (the radius is determined by the quantity of gas available), whereas a model reaching the Strömgen radius is *radiation bounded* (the radius is determined by the rate of ionizing photons emitted by the central source). A density bounded model can be roughly thought of as a radiation bounded model from which the outer zones have been stripped away: since these zones are those where the low ionization ions are found, a density bounded model has lower absolute intensities and a higher average ionization degree than the corresponding radiation bounded model. The second possibility to model photon escape in a simple way is to assume that the cloud does not cover the whole solid angle around the ionizing source, but rather an angle $\Omega < 4\pi$, a situation expressed by stating that a *covering factor* is assumed; the covering factor is the fraction $cf = \Omega/4\pi$. The physical picture is that all the ionizing photons emitted along certain directions are completely trapped, whereas all those emitted in other directions freely escape; or, equivalently, that the model is radiation bounded along certain directions, and ‘extremely’ density bounded (in the sense that no gas at all is encountered) along the others. The model is still spherically symmetric because the two kinds of directions are assumed to be completely mixed. A model with $cf < 1$ has lower absolute intensities and the same ionization degree as the corresponding model with $cf = 1$, because low and high ionization degree zones are cut away proportionally. Real nebulae are probably intermediate between the two scenarios described: the gas ends up at different radii according to the direction

considered, possibly covering all the range between 0 and R_S .

Note that the simple relations between the properties of radiation and density bounded models, and between the properties of models with $cf = 1$ and $cf < 1$, hold only if all the other input parameters are left unchanged. In the actual modeling practice things are not so straightforward, since we might want to change simultaneously several input parameters depending on which constraints we adopt. For instance, if we want to reproduce a given total $I(\text{H}\beta)$ value to fit an observed H II region, and to this aim we compute a sequence of models with varying cf , the observational constraint on H β forces us to increase the ionizing flux proportionally to the decrease in cf , and this change simultaneously yields changes in the local ionization degree.

2.3. Output quantities

For each model, we computed the intensities of the most important emission lines (H α , H β , [O III] $\lambda\lambda$ 5007, 4363, [O II] $\lambda\lambda$ 3727, 7325, [O I] λ 6300, [S II] $\lambda\lambda$ 6716, 6731, and He II λ 4686); the average temperatures $T_0(\text{H}^+)$, $T_0(\text{O}^+)$, and $T_0(\text{O}^{++})$ (hereinafter T_0 , T_{02} , and T_{03} , as in Paper I), with $T_0(\text{X})$ defined, for a given ion X, by the expression:

$$T_0(\text{X}) = \frac{\int_V T_e N_e N(\text{X}) dV}{\int_V N_e N(\text{X}) dV}, \quad (1)$$

where T_e is the electron temperature, N_e the electron density, $N(\text{X})$ the ionic density, and V the observed volume; the ‘empirical’ [O III] temperature $T(4363/5007)$ (hereinafter $T(\text{O III})$) obtained from the standard relation applied to the predicted λ 4363/ λ 5007 ratio; the ‘empirical’ [O II] temperature $T(3727/7325)$ (hereinafter $T(\text{O II})$), obtained from the expression

$$T(\text{O II}) = T_{02} \left[1 + \left(\frac{97,300}{T_{02}} - 3 \right) \frac{t_2^2}{2} \right] \quad (2)$$

(Peimbert 1967); the temperature fluctuation parameters $t^2(\text{H}^+)$, $t^2(\text{O}^+)$, and $t^2(\text{O}^{++})$ (hereinafter t^2 , t_2^2 and t_3^2 , as in Paper I), with $t^2(\text{X})$ defined as

$$t^2(\text{X}) = \frac{\int_V [T_e - T_0(\text{X})]^2 N_e N(\text{X}) dV}{T_0(\text{X})^2 \int_V N_e N(\text{X}) dV}; \quad (3)$$

the ionization fraction O^+/O , defined as

$$\text{O}^+/\text{O} = \frac{\int_V N_e N(\text{O}^+) dV}{\int_V N_e [N(\text{O}^+) + N(\text{O}^{++})] dV}, \quad (4)$$

called α in Paper I; the related quantity¹ $O^{++}/O = 1 - O^+/O$; and the helium ionization correction factor, $icf(\text{He})$, defined by the relation:

$$\begin{aligned} \frac{N(\text{He})}{N(\text{H})} &= \frac{\int N_e N(\text{He}^0) dV + \int N_e N(\text{He}^+) dV + \int N_e N(\text{He}^{++}) dV}{\int N_e N(\text{H}^0) dV + \int N_e N(\text{H}^+) dV}, \\ &= icf(\text{He}) \frac{\int N_e N(\text{He}^+) dV + \int N_e N(\text{He}^{++}) dV}{\int N_e N(\text{H}^+) dV}. \end{aligned} \quad (5)$$

The emission spectrum and the other computed quantities of each model were modified to simulate the bias introduced by the angular extension of the slits used in the observations. This step is crucial in the modeling, since the observed emission spectrum depends strongly on the portion of the nebula included in the aperture, as a consequence of the ionization and temperature structure of the nebula: see a thorough discussion and multiple examples of this effect in Luridiana et al. (1999) and Luridiana & Peimbert (2001).

The output quantities fall in three distinct categories: the first group includes those quantities that are computed to be compared with the corresponding observational constraints, and their agreement determine whether the fitting procedure is converging or not; this is the case of the line intensities, and of $T(\text{O II})$ and $T(\text{O III})$, which are the theoretical quantities that correspond to the observed temperatures derived from the line ratios $[\text{O II}] \lambda 3727 / \lambda 7325$ and $[\text{O III}] \lambda 4363 / \lambda 5007$. To this respect, note that the intensities of the helium lines have not been included in the set of observational constraints because they are not useful for this scope: as all the recombination lines arising from a dominant ion, they are very weakly dependent on the features of the model. The second group includes those output quantities computed with the aim of obtaining an information that is not available from observations: this is the case of $icf(\text{He})$, whose predicted value is assumed to be equal to the actual one, and is used to compute the total helium abundance. Finally, the remaining quantities are computed either for information, or because they are necessary to compute other predicted quantities: for example, T_{02} and t_2^2 are used to compute the predicted $T(\text{O II})$ by means of equation (2). The average temperatures T_0 , T_{02} , and T_{03} and the temperature fluctuations parameters t^2 , t_2^2 , and t_3^2 give a measure of the temperature structure of the models, and describe how it compares with the temperature structure of the actual region.

¹Note that these quantities are *not* the same as those listed in the ‘Log10 Mean Ionisation (over volume)’ block at the end of the output of Cloudy 94, which are simple volume averages of the ionization fractions; in the case of non-constant density the two definitions do not coincide. For an outward-decreasing density law, Cloudy’s definition yields lower fractions for the high ionization degree ions.

As a rule, t^2 , t_2^2 , and t_3^2 always turn out to be smaller than the corresponding empirical quantities. Analogously, T_{02} and T_{03} are always smaller than $T(\text{O II})$ and $T(\text{O III})$ respectively, unless $t_2^2 = 0$ or $t_3^2 = 0$; see Peimbert (1967) and Paper I for more details.

2.4. Observational constraints

The basic conceptual step in the fitting procedure is the comparison between the observed line intensities to the value predicted by our models. In this comparison, the largest weight is given to $\text{H}\beta$, $[\text{O III}] \lambda 5007$, and $[\text{O II}] \lambda 3727$, for the following two reasons: first, these lines are among the brightest of the spectrum, so they carry the smallest errors; second, they define the energetics and the ionization structure of the region, giving a first-order description of its overall structure. On the other hand, $[\text{O III}] \lambda 4363$ is not a robust constraint, because it may be affected by heating processes other than photoionization (see, e.g., Stasińska & Schaerer 1999); the intensity of $[\text{O I}] \lambda 6300$ depends strongly on the detailed description of the outer parts of the nebula, and is enhanced by the occurrence of filaments and clumps; finally, the detailed modeling of $\text{He II} \lambda 4686$ is not possible yet. This line forms in the recombination of He^{++} , an ion that can be produced potentially by different sources of radiation, and each candidate source poses a different problem that makes difficult to estimate quantitatively its relation to the nebular $\lambda 4686$ line. The most plausible sources of He^{++} are the hard radiation field of WR stars and the X-ray emission produced in the burst. WR stars, which are revealed by broad emission features in the spectrum, are not univocally associated to nebular $\lambda 4686$ emission, since in some cases they are observed with no associated nebular $\lambda 4686$ line, and in other cases the nebular $\lambda 4686$ is observed without detected WR stars; furthermore, the WR formation mechanism at low metallicities is still poorly understood, and standard evolutionary models systematically underpredict their number (see, e.g., the case of I Zw 18: Brown et al. 2002). The second candidate, X-ray emission, can be in turn ascribed to different sources: massive binary systems, supernova (SN) remnants, and the reprocessing of the gas kinetic energy in the interstellar medium. As for the first of these sources, the expected number of massive X-ray binaries is roughly 4 percent of the number of newly formed O stars (David, Jones, & Forman 1992); a similar fraction is also obtained by means of theoretical estimations (M. Cerviño, M. Mas-Hesse, & D. Kunth, in preparation; see also Mas-Hesse et al. 1996). The presence of massive X-ray binaries also implies the existence of SN remnants, which are a further source of He^{++} ; for both these sources to be present, the age of the burst must be larger than 3 Myr. Finally, the conversion of kinetic energy in X rays can be modeled assuming an efficiency factor, which can be estimated from the size of the bubbles in the region and from quantitative X-ray observations. Unfortunately, these data are not available for the H II regions considered in

this work, with the only exception of I Zw 18, where X rays have been detected (Stevens & Strickland 1998).

This brief discussion illustrates the difficulty of using the nebular $\lambda 4686$ intensity to constrain the properties of the cluster. This difficulty is increased by the statistical dispersion in both the number of WR stars and of X-ray sources (Cerviño, Mas-Hesse, & Kunth 2002): this implies that, even if the quantitative relation between a particular source and the intensity of $\lambda 4686$ were perfectly known, there would still be a residual uncertainty in the modeling of those regions where sampling effects are relevant.

2.5. Collisional effects

The effects of the collisional enhancement of Balmer lines on the determination of Y_P have already been discussed by several authors: see, for example, Davidson & Kinman (1985), Skillman & Kennicutt (1993), Stasińska & Izotov (2001), and Peimbert et al. (2002). This section will give a general overview of the problem, and describe the particular strategy followed in this work to give a quantitative estimate of the effect.

2.5.1. Theoretical overview

In H II regions, the main process contributing to the intensity of Balmer lines is H^+ recombination. Under appropriate physical conditions, a further contribution can arise from the cascade following the collisional excitation of H^0 from the ground state to an excited level. This contribution is generally a minor one, both because the fraction of H^0 inside the H II region is very small, and because very few free electrons have energies sufficient to make ground-state H^0 electrons jump to excited levels in the typical conditions of H II regions (a minimum of 12 eV is required to produce $H\alpha$, more than that for the higher Balmer lines). Nevertheless, collisional enhancement of Balmer lines might reach a relative value of several percent. If not taken into account, the collisional contribution has two biasing effects on the determination of Y_P . The first is a straightforward consequence of the enhancement of the observed Balmer intensities: if the observed intensity is interpreted in terms of pure H^+ recombination, the He^+/H^+ abundance is underestimated. The second effect is a consequence of the different collisional enhancements suffered by $H\alpha$ and $H\beta$: since the relative collisional increase in $H\alpha$ is always larger than that in $H\beta$, the measured $H\alpha/H\beta$ ratio is larger than it would be without collisions, producing a spurious reddening in the Balmer spectrum that mimics a higher extinction (Ferland & Osterbrock 1985). This

extra-reddening, when not properly subtracted out from the observed reddening to get the true extinction, has different consequences on the abundance determination according to the wavelength considered: it enhances the ratio $I(\lambda)/I(\text{H}\beta)$ for lines blueward of $\text{H}\beta$, and decreases it for lines redward of $\text{H}\beta$. Since He^+/H^+ is generally obtained as the weighted mean of the helium abundances obtained by different line ratios, the net result of neglecting the effects of collisional enhancement depends on which helium lines are used; in practice, it always traduces in a spurious Y decrease since the helium lines redward of $\text{H}\beta$ are globally brighter than those blueward of $\text{H}\beta$ (particularly $\text{He I } \lambda 5876$), and therefore are those that weigh the most in the analysis. An accurate determination of Y relies therefore on an accurate determination of the collisional effects affecting the line intensities of the region considered. This is in general a very difficult task, as we will make clear in the following.

The ratio between the collisional and the recombination contribution to the emissivity of a Balmer line, e.g. $\text{H}\alpha$, is related to the local conditions in the gas through the following expression (e.g., Osterbrock 1989):

$$\frac{j(\text{H}\alpha)_{\text{col}}}{j(\text{H}\alpha)_{\text{rec}}} \propto \frac{N(\text{H}^0)}{N(\text{H}^+)} \frac{e^{-\Delta E/KT_e}}{T_e^{1/2} \alpha(\text{H}\alpha)}, \quad (6)$$

where ΔE is the excitation energy of the upper $\text{H}\alpha$ level ($n = 3$) from the ground level ($n = 1$), and $\alpha(\text{H}\alpha)$ is the recombination coefficient. In this expression, we omitted those terms that are either constant or slowly varying with T_e . We also omitted the contribution to $j(\text{H}\alpha)_{\text{col}}$ from electrons excited to levels $n > 3$ that cascade down to $n = 3$ and finally produce an $\text{H}\alpha$ photon. Although simplified, this expression serves the scope of illustrating the difficulty of obtaining an accurate determination of collisional enhancement.

First, the ratio $j(\text{H}\alpha)_{\text{col}}/j(\text{H}\alpha)_{\text{rec}}$ is directly proportional to $N(\text{H}^0)/N(\text{H}^+)$, which is poorly known because it cannot be directly measured. The only possibility to estimate it is through a photoionization model; a very good model is needed to this scope, and it is important to assess to which extent the results obtained are model-dependent.

Second, the ratio $j(\text{H}\alpha)_{\text{col}}/j(\text{H}\alpha)_{\text{rec}}$ depends strongly on the temperature, particularly through the Boltzmann factor $\exp(-\Delta E/KT_e)$. This dependence poses a difficult problem, since most photoionization models underestimate the temperature observed in H II regions (e.g., Luridiana et al. 1999; Stasińska & Schaerer 1999; Luridiana & Peimbert 2001; but see also Oey et al. 2000 for a different result). This fact suggests that an extra-heating energy source is operating in H II regions. Several hypotheses have been proposed to explain the nature of such energy source, but none of them has yet found general agreement (e.g., Baldwin et al. 1991; Dopita & Sutherland 2000; Stasińska & Szczerba 2001; Luridiana, Cerviño, & Binette 2001). Most important, even the knowledge of the nature of the the extra-heating source would not probably imply a knowledge of the exact temperature structure,

and particularly its spatial correlation to the ionization structure, which enters equation (6) through the product of $N(\text{H}^0)/N(\text{H}^+)$ with the Boltzmann factor.

Finally, an important issue is the accuracy of the atomic parameters involved in the calculations. For the collisional transitions from the hydrogen ground level up to $n = 5$, Cloudy 94 uses the recent calculations by Anderson et al. (2000) and Anderson et al. (2002). Although these authors do not give any explicit number regarding the estimated accuracy of their calculations, they perform a comparison with previous results, finding differences smaller than 15 percent in the energy range of interest. Whether this number can be taken as a good measure of the current uncertainties, it is difficult to say; our impression is that the overall uncertainty introduced by atomic physics plays a minor role in this study.

2.5.2. *Observational constraints to collisional enhancement*

An upper limit to the collisional enhancement of Balmer lines is always implicitly defined by the observed reddening. This limit corresponds to the extreme case in which the internal extinction of the observed object, $C(\text{H}\beta)^{\text{int}}$, is negligible (with “internal extinction” meaning extinction caused by dust physically associated to the H II region, independently of it being mixed with the ionized gas or not), and is therefore equal to the collisional enhancement that would produce exactly the observed reddening, corrected for the Galactic intrinsic extinction $C(\text{H}\beta)^{\text{gal}}$: that is, if we define a collisional reddening coefficient as

$$C(\text{H}\beta)^{\text{col}} = \frac{\text{Log}(I(\text{H}\alpha)^{\text{tot}}/I(\text{H}\beta)^{\text{tot}}) - \text{Log}(I(\text{H}\alpha)^{\text{rec}}/I(\text{H}\beta)^{\text{rec}})}{-f(\text{H}\alpha)}, \quad (7)$$

where $I(\lambda)^{\text{tot}}$ and $I(\lambda)^{\text{rec}}$ are the total and the recombination intensities, and $f(\text{H}\alpha)$ is the value of the reddening function at $\text{H}\alpha$, then the observed reddening coefficient can be written as:

$$C(\text{H}\beta)^{\text{obs}} = C(\text{H}\beta)^{\text{gal}} + C(\text{H}\beta)^{\text{int}} + C(\text{H}\beta)^{\text{col}}, \quad (8)$$

thus

$$C(\text{H}\beta)^{\text{col}} \leq C(\text{H}\beta)^{\text{obs}} - C(\text{H}\beta)^{\text{gal}}. \quad (9)$$

In the following, by the expression “collisional reddening” we will always implicitly refer to the collisional reddening *of the Balmer lines*, and not to a global reddening affecting the whole spectrum.

It should be noted that the same line of reasoning exposed above could be applied to higher Balmer lines, with the aim of obtaining further constraints on collisional excitation. The amount of estimated collisions has a weaker direct influence on the derived $\text{H}\delta$ and $\text{H}\gamma$

intensities than in the case of $H\alpha$ and $H\beta$, since these lines have higher excitation thresholds. On the other hand, the degree in which collisions occur determines how much of the observed reddening is due to interstellar extinction, which in turn has an important impact on these lines: therefore, they can be in principle strong indicators of collisions through the indirect effect on the estimated extinction. However, they have also larger relative observational uncertainties as compared to $H\alpha$ and $H\beta$, so their actual power to put constraints on collisions depends crucially on the data quality. Since the whole procedure of estimating collisional contribution admittedly skates on thin ice, we chose in this work to rely solely on the more robust constraints provided by $H\alpha$ and $H\beta$.

2.5.3. The approach of photoionization modeling

In this work, our approach to the quantitative estimation of collisional enhancement is the following: first, for each object we compute a best-fit model that reproduces the observational constraints, paying particular attention to the ionization structure; second, we compute, for that particular model, the amount of collisional contribution to $H\alpha$ and $H\beta$; third, we assess in each case the uncertainty affecting our estimate of the collisional contribution. The last is by far the most difficult step, and there is no unique and completely safe way to undertake it. Our strategy to face this problem is to determine the range of collisional contribution spanned by satisfactory models of a given region (i.e., how much model-dependent is the collisional contribution), and the range of collisional contribution spanned by temperature-enhanced models. The temperature-enhanced models necessary to realize this last point have been computed with different modeling approximations. The outcome will be discussed in detail for the three cases in the next sections.

3. SBS 0335–052

SBS 0335–052 is the second most metal-poor galaxy known with $Z = 1/40 Z_{\odot}$, a metallicity only slightly higher than the one of I Zw 18. We will start our discussion with this object, because the observational constraints available for SBS 0335–052 are by far more numerous and articulate than for the other two objects. This fact allowed us to build more sophisticated models, and to determine in a more stringent way the collisional contribution to the Balmer lines and the corresponding uncertainties.

3.1. Observational constraints

SBS 0335–052 is a roundish region with a redshift $z = 0.0136$ (Izotov et al. 1997b), yielding a distance $d = 57$ Mpc for $H_0 = 72$ km s⁻¹ Mpc⁻¹. Izotov, Chaffee, & Schaerer (2001) report observations of ionized gas extending over a region of $\sim 26'' \times 32''$, corresponding to linear dimensions ~ 7200 pc \times 8800 pc, but the H β intensity falls to less than 1/100 of its peak value within a region of angular radius $\sim 3.5''$ (Figure 2a in Izotov, Chaffee, & Schaerer 2001), corresponding to a linear radius of ~ 1000 pc, so we will adopt this value as an approximate constrain on the radius.

The total H β flux² observed by Izotov et al. (1999) is $F(\text{H}\beta) = 5.93 \times 10^{-14}$ erg s⁻¹ cm⁻²; the actual flux is certainly higher, because the slit they used (a $1'' \times 5.4''$ extraction of a longer slit: see below) does not cover the whole nebula. The reddening coefficient $C(\text{H}\beta)^{\text{obs}}$ determined by Izotov et al. (1999) varies from 0.225 dex to 0.33 dex along the slit; we will adopt in the following the value $C(\text{H}\beta)^{\text{obs}} = 0.26$ dex, corresponding to the total $F(\text{H}\alpha)/F(\text{H}\beta)$ in the slit. Adding up the fluxes observed by Izotov et al. (1997b) and Izotov et al. (1999), and subtracting out the portion common to the slits used in the two works (which were perpendicular to one another), we derive as a lower limit to the total intrinsic flux emitted by the region $I(\text{H}\beta) \sim 2.16 \times 10^{-13}$ erg s⁻¹ cm⁻², or a luminosity $L(\text{H}\beta) \sim 8.4 \times 10^{40}$ erg s⁻¹. This luminosity corresponds to $Q(\text{H}^0) = 1.8 \times 10^{53}$ s⁻¹ ionizing photons; this number also is a lower limit to the actual number of ionizing photons emitted by the central source, both because it is derived from a lower limit on $I(\text{H}\beta)$, and because photons may leak out of the region without producing any H β . Adopting a conservative value of 20 percent photon leak, we estimate $Q(\text{H}^0) \gtrsim 2.2 \times 10^{53}$ s⁻¹. The root mean square (rms) density, derived from the observed H β flux, is $N_e(\text{rms}) = 4.8$ cm⁻³; for a filling factor $\epsilon \sim 0.01$, which is a typical value for giant H II regions, this would correspond to an average local (forbidden-line) density $N_e \sim 48$ cm⁻³. This agrees with the data reported by Izotov et al. (1999), who derived, from the [S II] 6717/6731 ratio, density values ranging from 500 cm⁻³ near the center to 10 cm⁻³ in the outer zone.

The nebular line He II $\lambda 4686$ is observed in SBS 0335–052, with an intensity relative to H β in the range (0.02 – 0.05) depending on the position, with the highest values observed in the brightest part of the nebula. As possible sources for He II $\lambda 4686$, Izotov et al. (1997b) consider WR stars, MS stars, and X-ray binaries. Since they do not observe any broad WR feature in the spectrum, and the hard emission from MS stars does not seem intense enough to produce the observed $\lambda 4686$ flux, these authors favor the hypothesis of X-ray binaries

²As customary, we will indicate with $F(\lambda)$ the observed fluxes, and with $I(\lambda)$ the dereddened (intrinsic) fluxes, both in units erg s⁻¹ cm⁻².

(however, they do not consider the X rays produced by stellar winds and SN explosions through the release of kinetic energy, neither the X-ray emission of SN remnants, although the presence of X-ray binaries implies, at least, one previous SN explosion: see the discussion in Section 2.4). An additional argument invoked to rule out WRs is the spatial distribution of $\lambda 4686$ across the nebula, which is displaced from the other nebular lines; indeed, Izotov, Chaffee, & Schaerer (2001) find a spatial correlation of the line intensity with the position of a supershell that is probably a shocked region. a more general argument is that WRs formed through single-star evolution are expected to be very rare at extremely low metallicities. Nevertheless, the spectra taken by Izotov et al. (1999), at a position angle perpendicular to the previous one, show a weak bump around $4620 - 4640 \text{ \AA}$, suggesting the presence of WR stars, probably of the WN type. In this work, we do not make any attempt to reproduce the nebular $\lambda 4686$, due to the loose connection between the WR stars and nebular $\lambda 4686$ emission that has been discussed in Section 2.4. On the other hand, we take advantage of the observed stellar WR features to constrain the age of the region; if the WRs of SBS 0335–052 have formed through the standard, single-evolution channel, the region must be about 3 Myr old.

The observational constraints used in our modeling are the line ratios obtained by Izotov et al. (1999) with the Low-Resolution Imaging Spectrometer of the Keck II telescope. They used a $1'' \times 180''$ slit, centered on the second brightest cluster of the region and oriented SW-NE. From this slit, nine extractions of size $1'' \times 0.6''$ were obtained. Our aim is to reproduce the line ratios in the nine extractions simultaneously; this corresponds to a formidable number of independent, but interrelated, observational constraints, which altogether provide a much firmer handle on the inner structure of the nebula than the integrated properties.

3.2. The models of SBS 0335–052

3.2.1. General features

Our models of SBS 0335–052 are spherically symmetric and have a Strömngren radius of approximately $R_S \sim 1000 \text{ pc}$. We assume $Z_* = 0.001$ and $Z_{gas} = 0.0005$ for the stellar and gas metallicity respectively. Since the region is very large, and the stars appear scattered all over the projected surface (although they are preferentially concentrated towards the center), we assume that the star formation is going on in a continuous burst, which began $t = 3.0 \text{ Myr}$ ago. To compute the ionizing spectrum, we adopted the following procedure: we performed 100 Monte Carlo simulations with 2×10^4 stars each, assuming an IB case with a time step of 0.1 Myr; each cluster was evolved up to 3.0 Myr. The resulting mean mass of these synthetic clusters is $1.18 \times 10^5 M_\odot$ in the range $2 - 120 M_\odot$. In order to obtain the spectrum of a

CSF burst, these simulations have been summed over time taking randomly a Monte Carlo simulation for each age. The mean total stellar mass of the synthetic clusters is $3.5 \times 10^6 M_{\odot}$, which gives a CSF rate of $1.18 M_{\odot} \text{ yr}^{-1}$. Due to the large total mass of this region, the statistical fluctuations in the sampling of the IMF are very small, and the resulting ionizing spectrum obtained with this procedure is almost identical to the one computed assuming a completely sampled IMF.

We adopt as a lower limit to the number of ionizing photons $Q(\text{H}^0) = 2.2 \times 10^{53} \text{ s}^{-1}$, a choice leaving us the possibility to increase it to improve the fit of any given model (see Section 3.1); this does not pose any theoretical problem from the point of view of the IMF sampling, because the IMF is well sampled. In the gas we assume scaled-down solar abundances for all the heavy elements, with the exception of nitrogen and carbon: for these elements, the adopted abundances relative to solar are 1/160 and 1/120 respectively. The helium abundance is $N(\text{He})/N(\text{H}) = 0.076$.

3.2.2. The Gaussian model

The starting point for our computations was a radiation bounded model with constant density $N_e = 50 \text{ cm}^{-3}$, filling factor $\epsilon = 0.01$, and covering factor $cf = 1.00$. Based on this reference model, we computed sequences of models varying several parameters: Z_{gas} , ϵ , cf , and the density law; both constant and non-constant density laws were considered, with the last case represented by a Gaussian law: $N_e = \max(N_e^{\text{max}} \exp(r/r_0)^{-2}, N_e^{\text{min}})$.

The output of each model is modified to simulate observations through the nine extractions of the slit used by Izotov et al. (1999) (Figure 1). Most of the weight in the comparison is given to the three most central extractions, since their line intensities have the smallest errors. The best-fit model obtained from this grid of models, called hereinafter ‘Gaussian model’, has the following characteristics: $Z_{\text{gas}} = 0.0007$; Gaussian density law, with $N_e^{\text{max}} = 720 \text{ cm}^{-3}$, $N_e^{\text{min}} = 90 \text{ cm}^{-3}$, and $r_0 = 375 \text{ pc}$; $\epsilon = 6.4 \times 10^{-4}$; $cf = 0.80$. The remaining parameters are the same as in the reference model described above.

Figure 2 shows the comparison between the observed and the predicted line profiles for this model; the points correspond to the line intensities either observed or predicted in each of the nine extractions making up the slit. The model is, by construction, symmetric with respect to the center, whereas the observed profiles show mild asymmetries: in the modeling, a fit is considered satisfactory whenever the predicted point at any given radius reproduces the average observational point at that radius, obtained averaging the corresponding SW and NE values; the observational uncertainties are shown as errorbars superposed on the

observed profiles. The top panel shows the $H\beta$ intensity, which is, within the observed uncertainties, very well reproduced by the model. Nevertheless, the three bottom panels show large discrepancies in the projected radial behavior of the ionization degree. These discrepancies are of special concern because an accurate estimate of collisions requires reproducing the ionization structure of the observed region. The observed ionization degree is almost constant across the region, a condition which is difficult to reproduce with a radiation bounded, spherical model with a central source of radiation. Physically, the observed profiles can be explained in several ways, for example: (i) the region is density bounded, so the low-ionization zone is cut off; (ii) the local density in the outer zones is much lower than assumed by our model, implying a drop in the local recombination rate and, consequently, a higher ionization degree in the outer zones; (iii) the ionizing stars are scattered throughout the region, each creating its own smaller H II region with high- and low-ionization zones, the complex of H II regions merging with each other.

Alternative (i) can be excluded on the basis of the relatively low ionization degree, since in a density bounded region the ionization degree is smooth but high. Alternative (ii) would imply a simultaneous increase in the filling factor of the outer zones, to preserve the observed $H\beta$ flux; but such possibility is not too appealing, since the scarce observational evidence regarding this point seems to suggest either the opposite behavior, or a nearly constant filling factor (e.g., Osterbrock 1989). Furthermore, the outer density of the Gaussian model is already quite low, so that no much room is left for lowering it further. Alternative (iii) is supported by a cursor inspection of direct images of SBS 0335–052 (see, e.g., Thuan, Izotov, & Lipovetsky 1997), and is also the most consistent with the scenario of a CSF burst. Direct images also show that the density structure of the region is filamentary, rather than smooth. To take these facts into account and obtain a better fit, we built a more complicated model that simulates the filamentary distribution of the gas inside SBS 0335–052, and the distribution of the ionizing sources across the cloud. This model will be described in the next section.

3.2.3. *The multiple-shell model*

In this section we present a different model that improves the fit notably. The new model is the sum of a sequence of thin, constant-density shells, with different radii, and it will therefore be called ‘multiple-shell model’. Since three alternative versions of this model will be presented, all with the same geometrical layout, we will further refer to them as A, B, and C; multiple-shell model A is the reference one and is described in the following.

Each shell composing model A is in itself radiation bounded, and has $cf < 1$. In each

shell we could, in principle, independently vary the gas distribution (local density, filling factor, and covering factor); additionally, we could also vary the number of shells and their inner radii. We decided rather to fix *a priori* the number of shells, their inner radii, and the densities, pushed by several considerations: first, we tried to keep things as simple as possible. Second, the observational data and the modeling experience obtained with the Gaussian model provide a good initial guess for the density structure. Third, we want the shells to fill altogether the whole observed region, with no substantial gaps or underlapping, so that, when observed globally, the structure appears fairly smooth: this equals to a constraint on the outer radii, providing directly, with the further constraint on the density, the filling factor value for each region; the resulting filling factor values decrease smoothly in the outer direction, in agreement with some observational results (see Section 3.2.2). Fourth, in order to obtain a smooth structure without too many computational complications, we fixed the number of shells to be ten. The covering factor of each shell, which is left as a free variable, is a simple way to describe the filamentary structure of the region: at each radius, photons encounter voids and regions filled with gas, mixed up together (so that, at the macroscopic level of the slit, voids and clumps are intercepted proportionally to the volume they occupy globally). Finally, we still have to take into account that the ionizing stars are scattered throughout the nebula. This is not possible to compute directly with a 1D code as Cloudy (see Viegas 2003 for a discussion on the differences between 1D and 3D codes), so we resorted to the following approximation: as far as we proceed from the innermost to the outermost shell, we gradually increase the absolute luminosity of the ionizing source. This increase reflects the fact that, when stars are scattered throughout the nebula, the outer zones receive a higher flux relatively to the central zones than it occurs in the case of a central source. The absolute normalization is then achieved by tuning the covering factor of each shell. The resulting effective covering factor, obtained as the luminosity-weighted average of the covering factors of the individual shells, is $\langle cf \rangle = 0.22$. This shell structure gracefully reproduces the constancy of the ionization degree along the diameter of the nebula: this is a consequence of each shell having its own low- and high-ionization zones. At the same time, the $H\beta$ flux profile is equally well reproduced as in the Gaussian case, because the overall density structure is nearly the same. Figure 3 summarizes the input parameters of model A, and Figure 4 illustrates the line profiles obtained when the model is observed through the slit.

Table 1 compares the predicted spectrum to the observational constraints. The column header “Center” refers to the centermost extraction. The label “0”.6” indicates, in the case of ‘Observed’, the average intensities of the two neighbouring extractions (indicated as “0”.6SW” and “0”.6NE” in Table 2 of Izotov et al. 1999); in the case of ‘Predicted’, it indicates the intensities predicted for either of the two extractions situated on both sides of

the central extraction. “Complete slit” indicates the sum of the nine extractions. “Complete model” is given for reference, and it indicates the results for the complete model, with no aperture correction applied: no ‘Observed’ column exists in this case, since there are no observational data sampling the whole nebula. The meaning of the column headers is also visually explained by Figure 1. The observed $T(\text{O III})$ values have been computed from the line intensities of Izotov et al. (1999); we did not use the temperature values reported by these authors, since they only list them for single extractions, i.e. they do not give a value for the complete slit. For the same reason, the $T(\text{O II})$ values of Table 1 differ slightly from the corresponding ones given by Izotov et al. (1999), since we recalculated them in order to fill homogeneously all the slots of Table 1. In our calculation we assumed the same relation as Izotov et al. (1999) between $T(\text{O II})$ and $T(\text{O III})$, which is based on a fit to the photoionization models by Stasińska (1990). Finally, Table 2 contains various predicted quantities for model A, and Figure 5 compares the observed $[\text{S II}]$ 6716/6731 profile to the corresponding predicted values.

3.3. Collisional effects in SBS 0335–052

3.3.1. Model A

Table 1 shows that the model systematically underpredicts the temperature of the region. This disagreement has been a systematic feature in previous attempts of modeling H II regions (see Section 2.5), and can be ascribed to an additional energy source acting in photoionization regions, other than photoionization itself. It can be ignored in most cases when modeling an H II region, provided the relevant line ratios are reproduced; but for our aim, differences of $\sim 3,000$ K between the observed and the predicted temperature cannot be neglected, because collisional rates are so sensitive to the temperature. It is therefore necessary to assess how the difference in temperature between the model and the real region affects the collisional enhancement of hydrogen lines: this problem is the topic of next section.

3.3.2. Models B and C

Starting from the multiple-shell model A, we follow two different strategies to estimate how the enhanced temperature would affect collisions. The first strategy consists in computing a new multiple-shell model, named ‘model B’, identical to model A in all respects, with the only exception of the metal abundances, which have been reduced by 1/100; in

this way, we suppress almost completely the cooling due to metals and obtain higher temperatures. An important feature of this model is that the line profiles are the same as in model A, ensuring that the ionization structure of model B is the same as in model A; this, in turn, ensures that the dependency of the collisional rates on the ionization degree is well reproduced, a necessary ingredient to draw any conclusion on the relevance of collisions.

The second estimate of the effect of temperature on the collisional rates is a simple numerical experiment, consisting in recomputing the collisional rates at each point assuming a temperature 15 percent higher than the one of the original model. It should be emphasized that this is just a numerical trick and does not involve any change in the structure of the model: it does not even involve the computation of a new model, since its only effect is to output collisional rates computed with enhanced temperature values; the collisional rates used internally by the code to determine the equilibrium conditions are left unchanged. This implies that the computed collisional rates are *not* consistent with the model structure. We named this model ‘multiple-shell model C’.

3.3.3. Quantitative estimate of collisional enhancement in SBS 0335–052

Table 3 compares the relative contribution of collisions to the total $H\alpha$ and $H\beta$ intensity for the three multiple-shell models. Since model C is not self-consistent, its extremely high collisional rates (roughly twice those of model B, and four times those of model A) are probably an artefact. On the other hand, model B is totally self-consistent, its [O III] temperature is very close to the observed one, and so is the observed ionization structure along the slit. It seems reasonable therefore to assume that the collisional rates found for this model are a good estimate of the real ones. Since model B has almost no metals, its temperature is the highest achievable in a normal H II region with photoionization alone. This temperature is also the highest observed in H II regions (e.g., SBS 0335–052 is even hotter than I Zw 18): hence the collisional enhancement of this model possibly defines an upper limit to what occurs in real H II regions. It is important to stress that there is a completely independent argument supporting the last statement: since the collisional enhancement of Balmer lines mimics a higher extinction, the observed reddening values define implicitly an upper limit to the maximum amount of collisional enhancement of each object: see Section 2.5.2.

Considering the case of the complete slit, we find from Table 3 that the collisional contribution to $H\beta$ might range from a minimum of 2.1 percent to a maximum of 3.5 percent of the total intensity, with the corresponding contribution to $H\alpha$ varying from 7.4 to 11.7 percent. In the first case, the observed $F(H\alpha)/F(H\beta)$ ratio should be corrected by a factor

0.946, and in the second by a factor 0.915. The average $C(\text{H}\beta)^{\text{obs}}$ observed along the slit should therefore be decreased from the observed value 0.26 dex to a collision-corrected range (0.14 – 0.19) dex to get the true extinction. The collisional reddening coefficients computed for all the cases considered are listed in the last row of Table 3.

Reversing the reasoning, we could find a maximum collisional enhancement for the $\text{H}\alpha/\text{H}\beta$ ratio by assuming that the $C(\text{H}\beta)^{\text{int}}$ of the region is negligible. Correcting the $C(\text{H}\beta)^{\text{obs}}$ value with the galactic extinction value by Schlegel, Finkbeiner, & Davis (1998) ($E(B - V) = 0.047$, or $C(\text{H}\beta)^{\text{gal}} = 0.07$ dex), we find $C(\text{H}\beta)_{\text{max}}^{\text{col}} = 0.19$ dex. This amount of collisional reddening could be obtained with a 16 percent collisional enhancement in the ratio $I(\text{H}\alpha)/I(\text{H}\beta)$; this in turn would put a rough upper limit on the collisional enhancement equal to $I(\text{H}\beta)_{\text{col}}^{\text{max}}/I(\text{H}\beta)_{\text{tot}} = 0.05$, where it has been assumed, based on Table 3, that $I(\text{H}\alpha)_{\text{col}}/I(\text{H}\alpha)_{\text{tot}} \sim 3.5 \times I(\text{H}\beta)_{\text{col}}/I(\text{H}\beta)_{\text{tot}}$.

4. I Zw 18

I Zw 18 is the most metal-poor galaxy known, with $Z = 1/50 Z_{\odot}$. Given this extremely low metallicity value, it is a key object in the primordial helium analysis, and it has been studied by many authors. The redshift of the galaxy is $z = 0.00254$ (Izotov, Thuan, & Lipovetsky 1997), which gives a distance $d = 10.6$ Mpc for $H_0 = 72 \text{ km s}^{-1} \text{ Mpc}^{-1}$; its apparent size is roughly $5'' \times 10''$, corresponding to linear dimensions $250 \text{ pc} \times 500 \text{ pc}$ at the assumed distance. I Zw 18 is made up of two main regions, usually referred to as the south-east (SE) and north-west (NW) knots. The NW region is more extended and globally brighter than the SE region: the $\text{H}\beta$ flux observed by Izotov et al. (1999) is $F(\text{H}\beta) = 2.08 \times 10^{-14} \text{ erg s}^{-1} \text{ cm}^{-2}$ in the NW knot³, and $F(\text{H}\beta) = 1.49 \times 10^{-14} \text{ erg s}^{-1} \text{ cm}^{-2}$ in the SE knot; the NW knot has been observed with a $4.2'' \times 1.5''$ slit, and the SE knot with a $3.5'' \times 1.5''$ slit. The nebular He II line $\lambda 4686$ is observed in I Zw 18, with $I(\lambda 4686)/I(\text{H}\beta) = 0.041$ in the NW region, and 0.009 in the SE region (Izotov et al. 1999); Vílchez & Iglesias-Páramo (1998) observe $\lambda 4686$ emission throughout the whole galaxy, with intensities relative to $\text{H}\beta$ ranging from 0 to 0.080. The spectra of the NW knot show evidence of WR stars (Izotov et al. 1997a; Legrand et al. 1997; Brown et al. 2002), whereas no stellar WR features have been observed to date in the SE knot.

In this work we model the emission from the SE knot; although less conspicuous than the NW knot, the SE knot is less affected by underlying absorption in the helium lines, and

³The value published in the paper, $F(\text{H}\beta) = 1.04 \times 10^{-14} \text{ erg s}^{-1} \text{ cm}^{-2}$, is an erratum (Y. I. Izotov 2003, private communication)

is therefore more suitable for a precise determination of the helium abundance in the galaxy. As a drawback of this choice, it turns out to be quite difficult to estimate the age. Our assumptions regarding this point will be discussed in the next section.

4.1. Observational constraints

4.1.1. Line intensities and physical conditions

We used as observational constraints the line intensity ratios by Izotov et al. (1999). As in the case of SBS 0335–052, we modified the model’s output to take into account the $1.5'' \times 3.5''$ slit used by Izotov et al. (1999), which samples, at the assumed distance, a region of $77 \text{ pc} \times 180 \text{ pc}$.

The total $H\beta$ flux observed by Izotov et al. (1999) is a lower limit to the total $H\beta$ flux emitted by the SE knot, since the SE knot has a diameter of approximately $4''$. To estimate the total flux, we compared Figure 1 in Izotov et al. (1999) to Figure 3 in Cannon et al. (2002). The comparison suggests that the slit used by Izotov et al. (1999) covered the regions labeled SE D1, SE D4, SE D5, SE D6, and SE D7 by Cannon et al. (2002) (although no precise correspondence can be established, due to the scale of the figures and the seeing, which was equal to the width of the slit). The sums of the corresponding $H\beta$ fluxes coincide to better than 15 percent, providing a consistency check for this assumption. Therefore, we will adopt for the total $H\beta$ flux emitted by the region the one given by Cannon et al. (2002) for the 8 clumps labeled “SE D1” through “SE D8”, which is 23 percent higher than the one measured by Izotov et al. (1999).

Consistently with our assumption on the total observed $H\beta$ flux, we computed the total $I(H\beta)$ as the sum of the $F(H\beta)$ values observed by Cannon et al. (2002), each corrected for the corresponding extinction value; we obtain $I(H\beta) = 2.32 \times 10^{-14} \text{ erg s}^{-1} \text{ cm}^{-2}$, a value 56 percent higher than the one by Izotov et al. (1999).

4.1.2. Stellar population

The values of $\text{Log } Q(H^0)$ estimated from the $H\beta$ flux, together with reasonable assumptions on the covering factor ($0.40 \lesssim cf \lesssim 1.0$), range from 50.8 to 51.2; this would correspond to a total amount of gas transformed into stars of $4.2 \times 10^3 \lesssim M/M_\odot \lesssim 6 \times 10^4$ in the mass range 2–120 M_\odot . The lower limit corresponds to a 2 Myr burst with $\text{Log } Q(H^0) = 50.8$, or about 7×10^2 stars, and the upper limit to a 5 Myr burst with $\text{Log } Q(H^0) = 51.2$, or

about 10^4 stars. Because these values are quite small, sampling effects in the IMF cannot be neglected. The absence of WR stars in the cluster cannot be used to bracket the age, since the models predict, in the most favorable case, 1.6 WR stars on average and a probability of 20 percent of observing no WR stars; thus, we have no way of knowing whether no WR stars are observed because of the age or because of stochastic effects. Additionally, the spectra of the region show no evidence of Balmer jump (Garnett et al. 1997), ruling out the presence of old post-MS luminous stars. Based on these pieces of evidence, we have assumed that the main stellar population is composed of MS stars, and have explored relatively young populations ($2.0 \text{ Myr} \lesssim t \lesssim 3.7 \text{ Myr}$).

4.1.3. Reddening coefficient

The reddening coefficient in I Zw 18 varies strongly from knot NW to knot SE, and within the same knot. For example, recently determined values for the NW knot range from $C(\text{H}\beta) = 0.010$ (Skillman & Kennicutt 1993), to 0.011 (Izotov et al. 1997), 0.040 (Izotov & Thuan 1998), and 0.115 (Izotov et al. 1999), while those for the SE knot range from $C(\text{H}\beta) = 0.20$ (Skillman & Kennicutt 1993), to 0.265 (Izotov & Thuan 1998) and 0.015 (Izotov et al. 1999). Recently, Cannon et al. (2002) observed I Zw 18 with the HST/WFPC2 finding $C(\text{H}\beta)$ values in the (0.00 – 0.18) range for the NW knot, and in the (0.00 – 0.27) range for the SE knot. The average extinction coefficient for these data is $C(\text{H}\beta) = \text{Log}[I(\text{H}\beta)/F(\text{H}\beta)] = 0.10$ dex.

4.2. The models of I Zw 18

In our models of I Zw 18 we assume an IB star-formation law; to obtain the spectrum, we have performed 100 Monte Carlo simulations of clusters with 1×10^3 stars, yielding a mean mass of $5.8 \times 10^3 M_{\odot}$. The complete set of simulations is shown in Figure 6. In the figure we also show for comparison the results of the analytical simulation corresponding to the same parameters. As expected, the analytical simulation gives an intermediate value with respect to the ensemble of Monte Carlo simulations. Since the ionizing flux in I Zw 18 is quite hard, and since the probability of obtaining a cluster in the upper tail of the Monte Carlo distribution is small but appreciable, we have chosen for our modelization one of the harder spectra.

Our best-fit model for I Zw 18 has been obtained with a $t = 3.2 \text{ Myr}$ spectrum, which is shown with a bold line in Figure 6 (note that the figure only represents the stellar spectrum

without the nebular contribution, which could cancel out the Balmer jump); this spectrum gave the best results of several alternative spectra that have also been tried. In analogy to the case of SBS 0335–052, this model has been named model A. The nebular parameters for the model A of I Zw 18 are the following: $Z_{gas} = 0.0005$; Gaussian density law with $N_e^{\max} = 150 \text{ cm}^{-3}$, $N_e^{\min} = 20 \text{ cm}^{-3}$, and $r_0 = 20 \text{ pc}$; $\epsilon = 0.15$; $cf = 0.55$; the chemical composition described above; and a Strömgren radius $R_{\text{out}} = 77 \text{ pc}$. Table 4 compares the predicted nebular spectrum to the observational constraints. The observed and predicted $T(\text{O II})$ and $T(\text{O III})$ values are also listed.

4.3. Collisional effects in I Zw 18

Table 4 compares the observed to the predicted temperatures for I Zw 18; the observed $T(\text{O II})$ and $T(\text{O III})$ values have been taken from the paper by Izotov et al. (1999). The predicted temperatures are smaller than the observed ones, as it happens with SBS 0335–052, but the differences in this case are far more modest, amounting to a maximum of 250 K for the case of $T(\text{O II})$. Additionally, I Zw 18 is somewhat colder than SBS 0335–052, so the effect of collisions on hydrogen lines is expected to be smaller. Of bigger concern is the failure to fit the intensities of the low-ionization lines, such as the $[\text{O II}]$ and the $[\text{S II}]$ lines. However, in this case we have less stringent observational constraints than in the case of SBS 0335–052, and it is not possible to obtain a better model.

The effect of temperature on the predicted collisions was estimated following the same procedure as in the case of SBS 0335–052: a new model was computed, identical to model A in all respects with the exception of metallicity, which is set to 1/10 of the value assumed for model A. A lower scaling factor is sufficient in this case, because the difference between the model’s predictions and the observed temperatures are more modest than in SBS 0335–052. As a matter of fact, the new model – hereinafter model B, analogously to the nomenclature adopted for the models of SBS 0335–052 – turns out to be substantially hotter than I Zw 18. All the other predicted quantities are essentially the same as in model A, with the only obvious exceptions of the metal line intensities and the temperature-related quantities. The predicted temperatures and other quantities are listed in Table 5.

Table 6 compares the relative contribution of collisions to the total $\text{H}\alpha$ and $\text{H}\beta$ intensities for models A and B, and lists the values of the derived $C(\text{H}\beta)^{\text{col}}$. The galactic reddening towards I Zw 18 is $0 \text{ mag} \leq E(B - V) \leq 0.03 \text{ mag}$ according to Burstein & Heiles (1982), and $E(B - V) = 0.032 \text{ mag}$ according to Schlegel et al. (1998), yielding $C(\text{H}\beta)^{\text{gal}}$ values in the range (0.00 – 0.05) dex. The total observed reddening is $C(\text{H}\beta)^{\text{obs}} = 0.015 \text{ dex}$ according to Izotov et al. (1999), and $\langle C(\text{H}\beta)^{\text{obs}} \rangle = 0.10 \text{ dex}$ according to Cannon et al.

(2002) (Section 4.1.3). If we adopt $C(\text{H}\beta)^{\text{obs}} = 0.06 \pm 0.04$ dex and $C(\text{H}\beta)^{\text{gal}} = 0.025 \pm 0.025$ dex as estimates of the observed reddening and the galactic extinction, we find that the maximum amount of collisional reddening is $C(\text{H}\beta)_{\text{max}}^{\text{col}} \sim 0.035 \pm 0.045$ dex. The upper limit set by this estimate coincides with the value given by model B, and is only slightly larger than the value predicted by model A. These predictions can therefore be used to derive a reasonable estimate for the actual collisional enhancement of the SE knot in I Zw 18. The specific values assumed will be discussed in Section 6.2.

5. H 29

5.1. Observational constraints

H 29, also known as I Zw 36 and Mrk 209, is the third brightest H II region in the sample of 24 objects analyzed by Izotov et al. (1997), who measured $F(\text{H}\beta) = 1.46 \times 10^{-13}$ erg s⁻¹ cm⁻². The heliocentric redshift of this object is $z = 0.000937$ (de Vaucouleurs et al. 1991), which corresponds to a velocity relative to the Local Group centroid $v_{LG} = 349$ km s⁻¹; assuming $H_0 = 72$ km s⁻¹ Mpc⁻¹, a distance $d = 4.85$ Mpc is found. The FWHM radius in radio frequencies is $R \sim 30$ pc (Viallefond & Thuan 1983), while the region observed by Izotov et al. (1997) corresponds to a radius $R \sim 32$ pc (Section 5.1.2). According to the discussion on the observed H β flux in Section 5.1.2, the border of the ionized region must be somewhat bigger than this value, which we will take as a lower limit. No high quality data are available for H 29, for several reasons: the specific problems of each dataset will be discussed in the following.

5.1.1. Reddening coefficient

According to both Izotov et al. (1997) and Mas-Hesse & Kunth (1999), the observed reddening coefficient $C(\text{H}\beta)^{\text{obs}}$ is 0.00 dex, whereas Viallefond & Thuan (1983) found $C(\text{H}\beta)^{\text{obs}} = 0.41$ dex. While the first of these $C(\text{H}\beta)^{\text{obs}}$ values is probably an artefact of the observational errors and the underlying absorption in the Balmer lines, the second value is much too high: the detector used by Viallefond & Thuan (1983) was later found to be non-linear, and the intensities given in that paper must be corrected using the expression $S = F^{1.07}$, where S is the instrumental signal and F the actual flux (Torres-Peimbert, Peimbert, & Fierro 1989). After correcting the data by Viallefond & Thuan (1983) for non-linearity and assuming 2Å of underlying absorption in H δ , a revised value $C(\text{H}\beta) = 0.22 \pm 0.15$ dex is obtained. Combining this value with those by Izotov et al. (1997) and Mas-Hesse & Kunth (1999), we will

adopt as a rough estimate for the reddening $C(\text{H}\beta) = 0.07 \pm 0.08$ dex.

5.1.2. Line intensities and physical conditions

The line intensities by Izotov et al. (1997) have been adopted as observational constraints. The line intensities by Viallefond & Thuan (1983) suffer from several limitations, particularly the non-linearity of the detector and the large observational errors. The more recent data by Izotov et al. (1997) have smaller errors, but the slit they used ($2'' \times 3.5''$) does not cover the whole object. Comparing the $\text{H}\beta$ fluxes measured by Izotov et al. (1997) and Viallefond & Thuan (1983) (who used a circular slit with $6.1''$ diameter), and bearing in mind the uncertainties affecting the older data, it can be estimated that Izotov et al. (1997) collected approximately 90 percent of the total $\text{H}\beta$ flux emitted; thus, a reasonable estimate of the total dereddened $\text{H}\beta$ intensity, based on the $F(\text{H}\beta)$ value by Izotov et al. (1997) and the reddening coefficient derived above and corrected upwards by 10 percent, yields $I(\text{H}\beta) = (1.9 \pm 0.3) \times 10^{-13} \text{ erg s}^{-1} \text{ cm}^{-2}$. The rms density derived from $I(\text{H}\beta)$ is $N_e(\text{rms}) = 45 \text{ cm}^{-3}$. The forbidden-line density derived from the $[\text{S II}] 6716/6731$ ratio by either Viallefond & Thuan (1983) or Izotov et al. (1997) is $N_e(\text{rms}) \sim 100 \text{ cm}^{-3}$, implying an average filling factor $\epsilon \gtrsim 0.1$. Nebular $\text{He II } \lambda 4686$ emission in H 29 was observed by Izotov et al. (1997), with $I(\lambda 4686)/I(\text{H}\beta) = 0.012$; this line could be produced by WR stars, whose presence is revealed by a broad stellar feature around 4650 \AA . The modeling procedure is described in the next section.

5.2. The models of H 29

We computed for H 29 spherically symmetric photoionization models with $R_S \gtrsim 30 \text{ pc}$. The ionizing spectra were computed assuming an IB, and performing a sample of 100 Monte Carlo simulations with 4.5×10^3 stars; the mean mass of the clusters turned out to be $2.65 \times 10^4 M_\odot$. The complete set of simulations is shown in Figure 7. In the same figure we also show for comparison the results of analytical simulations.

In the models we adopted 1/10 solar abundances for all the heavy elements, with the exception of C, N, and O, for which we adopted abundances 1/35, 1/46, and 1/11 solar respectively, corresponding to $12 + \text{Log X/H} = 7.01, 6.31, \text{ and } 7.81$. The N and O abundances are taken from Izotov et al. (1997). For carbon there are no good determinations in H 29, so we adopted a C/O value typical of irregular galaxies in this metallicity range (Garnett et al. 1995, 1997). The helium abundance in the gas is $\text{He/H} = 0.078$ by number.

The observed total $H\beta$ intensity corresponds to a lower limit for the rate of ionizing photons given by $Q(H^0) \geq 1.1 \times 10^{51} \text{ s}^{-1}$; on the other hand, Viallefond & Thuan (1983) find, by means of radio observations, $Q(H^0) = 1.9 \times 10^{51} \text{ s}^{-1}$. Probably the radio observations include outer regions of H29 not included in the $H\beta$ measurements; therefore the comparison between these two figures gives $cf \leq 0.58$. In the modeling we assumed $cf = 0.50$.

With these parameters, several models were computed, varying the density law (either radially constant, or Gaussian: see Section 3), coupled to the filling factor to reproduce the observed radius. The best-fit model follows a Gaussian density law with $N_e^{\text{max}} = 250 \text{ cm}^{-3}$, $N_e^{\text{min}} = 40 \text{ cm}^{-3}$, and $r_0 = 15 \text{ pc}$; $\epsilon = 0.25$; $cf = 0.50$; the chemical composition described above; and a Strömngren radius $R_{\text{out}} = 55 \text{ pc}$. This model will be called model A for consistency with the nomenclature adopted in the previous cases; however, no enhanced-temperature alternative models have been computed in this case, as will be explained in the following. The predictions of this model will be presented without applying any aperture correction, since we assume that no significant portion of the region falls outside the slit. Table 7 compares the predicted spectrum to the observational constraints, and Table 8 contains various predicted quantities for model A.

5.3. Collisional effects in H 29

Table 7 summarizes the observed and predicted temperatures for H 29; the observed $T(\text{O III})$ temperatures have been taken from the paper by Izotov et al. (1999). As it happens with SBS 0335–052 and I Zw 18, the predicted temperatures are smaller than the observed ones; however, the differences in the case of H 29 are far more modest, amounting to a maximum of 650 K for the case of $T(\text{O III})$. Additionally, H 29 is much colder than SBS 0335–052, so the effects of collisions on hydrogen lines are certainly more modest, and an underestimation of the temperature has smaller consequences; for these reasons, we did not compute enhanced-temperature models for this region. Table 9 compares the relative contribution of collisions to the total $H\alpha$ and $H\beta$ intensity for the best-fit model, and lists the value of $C(H\beta)^{\text{col}}$ for the best-fit model. Although in the case of H 29 we cannot build a sophisticated model, due to the limitations in the observational constraints available, we are confident that the collisional contributions estimated by means of the model presented here are representative of the real situation, on the following grounds: first, the temperature of this region is quite low, so that collisions are not very important; second, the temperature of our model is a good approximation of the temperature of H 29; third, H 29 is small and compact, so that less structure than in the case of SBS 0335–052 is expected, making the need for spatially resolved observations less stringent; fourth, the reddening coefficient of this region is very

low, so that the upper limit on collisional enhancement placed by the observed reddening is also quite low. The galactic reddening towards H 29 is $0 \text{ mag} \leq E(B - V) \leq 0.03 \text{ mag}$ according to Burstein & Heiles (1982), and $E(B - V) = 0.015 \text{ mag}$ according to Schlegel et al. (1998), implying $C(\text{H}\beta)^{\text{gal}} = 0.02 \pm 0.02 \text{ dex}$. After subtracting this contribution from the total observed reddening $C(\text{H}\beta)^{\text{obs}} = 0.07 \pm 0.08 \text{ dex}$, we find that the maximum amount of collisional enhancement for the ratio $I(\text{H}\alpha)/I(\text{H}\beta)$ is 4 percent, implying a maximum collisional enhancement of 1.5 percent for $I(\text{H}\beta)$.

6. Effect of the collisional enhancement of the Balmer lines on Y_P

Davidson & Kinman (1985) pointed out that, in objects with high electronic temperatures, the lower Balmer lines may be collisionally enhanced. If the collisional contribution is not subtracted out from the total intensity of each line, it may result in spuriously low He/H ratios. Since high temperatures characterize low-metallicity objects, which are crucial for the determination of primordial helium, the derived Y_P is consequently underestimated. Davidson & Kinman (1985) estimated that the effect in I Zw 18 is roughly 2 percent for $I(\text{H}\alpha)_{\text{col}}/I(\text{H}\alpha)_{\text{tot}}$, and a third of that for $I(\text{H}\beta)_{\text{col}}/I(\text{H}\beta)_{\text{tot}}$.

The effect of collisional excitation of Balmer lines on the determination of Y_P has been discussed by several authors after Davidson & Kinman (1985) (Skillman & Kennicutt 1993; Stasińska & Izotov 2001; Paper I). Stasińska & Izotov (2001) remarked that, because collisions affect more H α than H β , collisions introduce an extra-reddening in the Balmer spectrum, which should be subtracted out before the abundance analysis is performed. Altogether, they estimate that neglect of collisional excitation of Balmer lines may result in an underestimate of Y_P by as much as 5 percent. In Paper I, the effect of collisional enhancement of Balmer lines was found to increase Y_P by +0.0028, corresponding to 1 percent. In the following, we will revise these results in the light of the improved models presented in this paper, and derive a new determination of Y_P .

6.1. Dust versus collisional effects

From an H α /H β map of I Zw 18 obtained from narrowband HST/WFPC2 images of the galaxy, Cannon et al. (2002) find that the H α /H β ratio was not homogenous, presenting values ranging from 2.75 to 3.40. After discarding several alternative explanations for these enhanced ratios, they interpret these variations in terms of dust patches in the galaxy. In particular, they argue against the possibility of collisional enhancement of H α /H β based on

the following line of reasoning: a) the highest ratios are observed in the SW knot, which is the one with the lower temperature; b) the observed ratios do not seem to follow any definite trend with the ionization parameter.

The line of reasoning expressed in the second point above might be challenged, based on the following considerations. In photoionization models, the collisional contribution reaches in general its maximum at some point halfway the center and the Strömngren radius, so the observed gradient depends on the exact interplay between T_e and the H^0/H^+ ratio of the particular model, with the projection and aperture effects taken into account. Thus, even for a model nebula, it would be extremely difficult to give a prescription for what the gradient in the collisional contribution is expected to be. One example is provided in Figure 8, which shows the behavior of various predicted quantities. The upper panel a) contains the radial behavior of the ratio between the collisional and the recombination emissivities of $H\alpha$ and $H\beta$; note the abrupt rise of the curves near the Strömngren radius, which is a consequence of the increase in the fraction of neutral hydrogen outweighing the fall in temperature. Panel b) shows the incremental contribution of each shell to the total luminosities, with the volume factor taken into account; to translate this figure into an observational prediction, one should further consider the projection effect, which in turn depends on the aperture; nevertheless, the bumps in the plot makes it clear that the dependence of luminosity on radius is something difficult to figure out a priori. Finally, panel c) illustrates the radial behavior of the hydrogen ionization fractions, and panel d) the radial behavior of the electron temperature and density. In the case of a real nebula, it is only reasonable to assume that things are far more complicated, and no specific shape for the gradient can be expected. One consideration supporting this conclusion is that the individual H II regions of different stars or small star clusters merge with one another, a fact that makes it even more difficult to make small-scale predictions on the radial behavior of any quantity. More in general, the concept of ionization parameter is tricky and should be used with caution: one reason is that several alternative definitions exist, and it is not always clear which one is being used; a second fact to consider is that most of them refer to the simplest cases of a central ionizing source and constant gas density, and things can change a lot when these hypotheses are relaxed. In short, if the concept of ionization parameter is used as a synonym of global ionization degree, it would be better to use the last expression, since it is more precise and univocal; if it refers to something else, it should be specified which definition is being used, and how it can be applied to the case of a real nebula with spread-out ionizing sources and radially changing density and filling factor.

Nevertheless, we agree with the conclusions by Cannon et al. (2002), that the main process causing $H\alpha/H\beta$ to depart from its theoretical value is dust extinction, on the following grounds: adopting for the expected recombination ratio $(H\alpha/H\beta)_{\text{rec}} = 2.76$ as in Cannon

et al. (2002), the individual ratios measured throughout the region differ from the expected ratio from a minimum of 0 to a maximum of 23 percent, averaging 8 percent. These values yield for the total reddening coefficients $C(\text{H}\beta)^{\text{obs}}$ values from 0 to 0.27 dex. If an average foreground extinction $C(\text{H}\beta)^{\text{gal}} = 0.025$ dex is subtracted out (Section 4.3, which agrees with the estimate by Cannon et al. 2002), the residual reddening amounts to values ranging from 0 to 0.24 dex, averaging 0.07 dex. If we were to explain such reddening in terms of pure collisional enhancement, this effect would imply a 7 percent enhancement on average in the $\text{H}\alpha$ intensity – three times more than estimated by Davidson & Kinman (1985) –, and a 22 percent enhancement in the most extreme case – eleven times more than estimated by Davidson & Kinman (1985). This values seem too extreme, and support the conclusion by Cannon et al. (2002) of internal dust extinction.

6.2. Effect on the derived reddening

Summarizing the conclusions drawn in Sections 3.3, 4.3 and 5.3, we will correct the observed $C(\text{H}\beta)$ values for the three objects with our estimate of the collisional contribution. Table 10 lists the observed and collision-corrected reddening coefficients.

The uncertainties have been computed as follows: for the case of SBS 0335–052, we assumed as the best estimate for $C(\text{H}\beta)^{\text{col}}$ the values predicted with Model B, the one that best fits both the temperature and the ionization structure; the uncertainty on $C(\text{H}\beta)^{\text{col}}$ was assumed equal to the difference between the values predicted by models A and B. The $C(\text{H}\beta)^{\text{obs}}$ values were formally derived from the published line fluxes.

For the case of I Zw 18, we assumed the $C(\text{H}\beta)^{\text{col}}$ value obtained with model A: we did not adopt the higher value given by model B, as in the case of SBS 0335–052, because model B is hotter than the observations (Section 4.3), and because the predicted collisional enhancement would be too high as compared to the observed reddening: see Section 4.3. The uncertainty on $C(\text{H}\beta)^{\text{col}}$ was assumed equal to the difference between the values predicted by models A and B. The assumed $C(\text{H}\beta)^{\text{obs}}$ value is the one inferred from the data by Cannon et al. (2002), and the uncertainty by Izotov et al. (1999) was assumed.

For the case of H 29 we assumed the $C(\text{H}\beta)^{\text{col}}$ value obtained with model A, and assumed the same uncertainty as in I Zw 18. This choice is somewhat arbitrary, but it is supported by the following considerations: first, the observational data available to constrain models of H 29 are scarce and not high-quality; second, the temperatures of the model are in fair agreement with the observed ones: hence, it is reasonable to assume that the absolute uncertainty affecting our estimation should not be too large; third, the temperatures (both

observed and predicted) are quite low in absolute terms, so it would be unreasonable to assume a large collisional contribution, as it would be implied by a large uncertainty; fourth, a larger uncertainty would contradict the assumed $C(\text{H}\beta)^{\text{obs}}$ value. As for $C(\text{H}\beta)^{\text{obs}}$, the assumptions underlying the number quoted have already been discussed in Section 5.1.1.

7. Determination of Y and Y_P

In this section, we will redetermine the helium abundance in the three H II regions, taking into account the collisional contribution to the Balmer lines. We will then show how the revised determination affects the derived Y_P value.

7.1. Helium abundances

As discussed in Section 2.5.1, the abundance analysis of H II regions can suffer from a bias if the collisional enhancement of hydrogen lines is neglected. The bias arises from two different effects: the first is an overestimation of the hydrogen recombination intensity, from which an underestimation of the He^+/H^+ ratio directly descends; the second effect is a consequence of the collisional reddening of the Balmer spectrum, which causes an overestimation of the extinction, and therefore an underestimation of the intensity of the red helium lines. Both effects act in the same direction, increasing the value of Y : they will be illustrated quantitatively in this section, where we present three different determinations of the helium abundance. In the first we neglect the collisional effects in the hydrogen lines; in the second we subtract the collisional contribution from the observed $I(\text{H}\beta)$, but we neglect the collisional effects on the observed reddening; finally, in the third we subtract the collisional contribution from both $I(\text{H}\beta)$ and $C(\text{H}\beta)^{\text{obs}}$.

In addition to the collisional contribution to the Balmer lines, to obtain He^+/H^+ values we need a set of effective recombination coefficients for the helium and hydrogen lines, an estimate of the optical depth effects for the He I lines, and the contribution to the He I line intensities due to collisional excitation. As in Paper I, we used a maximum likelihood method (MLM) to derive the He^+/H^+ values. We used the hydrogen recombination coefficients by Storey & Hummer (1995), and the helium recombination coefficients by Smits (1996) and Benjamin, Skillman, & Smits (1999). The collisional contribution to the He I lines was estimated from Sawey & Berrington (1993) and Kingdon & Ferland (1995). The optical depth effects in the triplet lines were estimated from the computations by Benjamin, Skillman, & Smits (2002). To obtain the $\text{He}^{++}/\text{H}^+$ values, we used the $I(4686)/I(\text{H}\beta)$ value together

with the recombination coefficients by Brocklehurst (1971). The total helium abundance was derived using equation (5) and the $icf(\text{He})$ values given by the models.

7.1.1. Helium abundance in SBS 0335–052

To derive He^+/H^+ in SBS 0335–052 we used the following inputs to the MLM (see Paper I): $\tau(3889) = 1.26 \pm 0.63$, $t^2 = 0.020 \pm 0.007$, and the He I fluxes at $\lambda\lambda$ 3889, 4026, 4471, 4922, 5876, 6678, and 7065 observed in the sum of the three centermost extractions of the slit used by Izotov et al. (1999). As in Paper I, the intensities of $\lambda\lambda$ 3889, 4026, 4471, 4922, and $\text{H}\beta$ have been corrected for underlying absorption following the prescriptions by González Delgado, Leitherer, & Heckman (1999). We did not use the theoretical t^2 derived in Section 3, since the values of Table 2 are lower limits to the real value (see Paper I).

Table 11 presents the values of the helium line fluxes, along with three sets of reddening-corrected line intensities. The $C(\text{H}\beta)$ values associated to each intensity set are also listed. The table also presents the y^+ and y^{++} determinations for each of the three cases. Finally, the last row presents the Y values derived for each case.

7.1.2. Helium abundance in I Zw 18

Following the same procedure used with SBS 0335–052, to derive He^+/H^+ we used the following data as inputs for the MLM (see Paper I): $\tau(3889) = 0.10 \pm 0.05$, $t^2 = 0.024 \pm 0.007$, and the fluxes of He I $\lambda\lambda$ 3889, 4026, 4471, 5876, 6678, and 7065 observed by Izotov et al. (1999). The intensities of $\lambda\lambda$ 3889, 4026, 4471, and $\text{H}\beta$ have been corrected for underlying absorption according to the work by González Delgado et al. (1999). We did not use the t^2 values of Table 5, since they are lower limits to the real values.

Similarly to Table 11, Table 12 presents the observed helium line fluxes from the observations of Izotov et al. (1999), along with three sets of reddening-corrected line intensities, the assumed reddening coefficients, and the values of y^+ , y^{++} , and Y determined through the MLM.

7.1.3. Helium abundance in H 29

The He^+/H^+ value in H 29 was derived using the following input data to the MLM: $\tau(3889) = 1.44 \pm 0.72$, $t^2 = 0.020 \pm 0.007$, $N_e = 175 \pm 50 \text{ cm}^{-3}$, and the observed fluxes of

He I $\lambda\lambda$ 3820, 3889, 4026, 4387, 4471, 4922, 5876, 6678, 7065, and 7281. The intensities of $\lambda\lambda$ 3820, 3889, 4026, 4387, 4471, 4922 and H β have been corrected for underlying absorption, according to the work by González Delgado et al. (1999). The t^2 listed in Table 8 were not used, since they are lower limits to the real value.

Table 13 presents the observed helium line fluxes taken from Izotov et al. (1997), along with three sets of reddening-corrected line intensities, the corresponding reddening coefficients, and the y^+ , y^{++} , and Y values derived for each line set.

7.2. Primordial Helium Abundance

To determine Y_P , it is necessary to estimate for each object the fraction of helium produced by galactic chemical evolution. We will assume that

$$Y_P = Y - O \frac{\Delta Y}{\Delta O}, \quad (10)$$

where O is the oxygen abundance by mass. The ΔO baseline given by the objects in this sample is very small and consequently produces large errors in the $\Delta Y/\Delta O$ determination: therefore we adopted $\Delta Y/\Delta O = 3.5 \pm 0.9$, a value based on observations and models of chemical evolution of irregular galaxies (Peimbert, Peimbert, & Ruiz 2000).

Equation (10) has induced researchers in this field to derive Y_P from the analysis of the most metal-poor extragalactic H II regions known, particularly I Zw 18 and SBS 0335–052, in an attempt to minimize the uncertainty of the determination. This is a valid procedure if one only considers the errors in the extrapolation to $O = 0.00$. Nevertheless, the collisional effect increases with the electron temperature, thus for very low metallicities the error due to collisions can become very large. In fact, the errors due to collisions for objects with $1/50 Z_\odot \lesssim Z \lesssim 1/25 Z_\odot$ can become larger than the errors due to the extrapolation for objects with $1/10 Z_\odot \lesssim Z \lesssim 1/5 Z_\odot$; therefore, the second set of objects allows to achieve a higher accuracy in the determination of Y_P .

From the sample made of the three objects SBS 0335–052, I Zw 18, and H 29 we derive the following results: (i) $Y_P = 0.2350 \pm 0.0028$, neglecting the collisional effects in the Balmer lines; (ii) $Y_P = 0.2380 \pm 0.0029$, subtracting the collisional contribution from the H β intensity, and neglecting the collisional effects on the observed reddening; (iii) $Y_P = 0.2403 \pm 0.0030$, correcting both $I(\text{H}\beta)$ and $C(\text{H}\beta)$ for collisional effects. This is, however, a very small sample: if we consider the larger sample presented in Paper I, which includes NGC 2363 and NGC 346 in addition to the regions studied in this work, the Y_P values obtained in the three cases become respectively $Y_P = 0.2356 \pm 0.0018$, $Y_P = 0.2377 \pm 0.0019$, and

$$Y_P = 0.2391 \pm 0.0020.$$

8. Discussion

There are three main procedures to estimate the collisional contribution to the hydrogen line intensities in giant H II regions. The first, which is observational, is the measurement of $C(\text{H}\beta)^{\text{obs}}$; the difference between $C(\text{H}\beta)^{\text{obs}}$ and $C(\text{H}\beta)^{\text{gal}}$ sets an upper limit to the amount of collisions; no lower limit can be found through this method. The second method is based on the use of generic grids of photoionization models; although this procedure allows establishing both a lower and an upper limit to collisional contribution, such limits are not necessarily more stringent than those set with the first method. Furthermore, this method gives no handle on the effect of temperature fluctuations, which is an important source of uncertainty. The third method is the computation of tailored photoionization models: although more precise than the use of generic grids of photoionization models, this method is extremely time-consuming; furthermore, it suffers from the same bias, since photoionization models are generally unable to reproduce the temperatures observed in actual H II regions. This difficulty may in some way be skipped by resorting to ingenious ways of taking the temperature bias into account, as we did in the cases of SBS 0335–052 and I Zw 18, but this procedure introduces an additional uncertainty that derives from the impossibility to predict the spatial correlation of the temperature to the ionization structure.

The best solution available at present is the simultaneous use of all the methods described above. This approach allows to put more stringent constraints on the amount of collisions than any of the individual methods taken separately; it also allows to estimate the uncertainty attached to these estimates in a relatively safe way, and to propagate it into the value of Y_P . A further refinement of this technique is at present impossible, and could come only from the availability of high-quality, spatially resolved data for a few selected objects: spatial resolution is necessary because it allows to compute better photoionization models.

From the point of view of the determination of Y_P , a different solution to the problem is to avoid the use of extremely low-metallicity objects, and to concentrate instead on obtaining high-quality data for an adequate sample of moderately low-metallicity objects. This solution was already hinted at by Peimbert (2003). Although for this class of objects the uncertainty on dY/dZ is amplified, the uncertainty introduced by collisions is smaller, with a global positive tradeoff.

9. Summary and conclusions

In this work, we presented tailored photoionization models for the three metal-poor extragalactic H II regions SBS 0335–052, I Zw 18, and H 29. In the modeling we put special care in the determination of the collisional contribution to the Balmer line intensities, and gave estimates of the uncertainties affecting such determination. An accurate determination of the collisional contribution to the Balmer lines requires a detailed modeling of both the temperature and the ionization structure of the nebulae. Although the uncertainties affecting these quantities are generally large, we showed in this work that the collisional contribution can be estimated in a rather precise way by means of the simultaneous use of alternative constraints. The most powerful constraint is provided by the observed reddening coefficient $C(\text{H}\beta)^{\text{obs}}$. In the three objects considered in this work the $C(\text{H}\beta)^{\text{obs}}$ values are quite low, putting a very stringent upper limit to the amount of collisions. This fact has an enormous importance from the point of view of helium determination: these three examples suggest that collisions are not as important as some previous analysis had suggested (e.g. Stasińska & Izotov 2001, who suggested that the $\text{H}\alpha/\text{H}\beta$ enhancement could reach values as high as 8 percent); more specifically, we can draw from this study quantitative conclusions on the correction to be applied to actual $Y_{\mathcal{P}}$ determinations, because our sample contains two of the objects that have played a determining role in the past determinations of $Y_{\mathcal{P}}$.

The main results of this study can be summarized as follows:

1. We present a set of tailored photoionization models for the three metal-poor extragalactic H II regions SBS 0335–052, I Zw 18, and H 29.
2. We computed for each model the collisional contribution to the $\text{H}\alpha$ and $\text{H}\beta$ intensities.
3. We discussed the different factors that could have an effect on our estimations, and for each object determined lower and upper limits on the percentage of the Balmer line intensities due to collisions.
4. We computed the helium abundances for each object, showing the effect of both neglecting and including Balmer line collisional effects in the analysis.
5. With the revised Y values for a sample of five extremely low- and moderately low-metallicity H II regions, we obtained a new determination of $Y_{\mathcal{P}}$. The difference with respect to the case in which collisions are neglected amounts to an upward change of +0.0035, yielding $Y_{\mathcal{P}} = 0.2391 \pm 0.0020$.

For future studies aimed at the determination of $Y_{\mathcal{P}}$, we make the two following remarks:

1. The use of low-metallicity objects requires obtaining high-quality, spatially resolved, and carefully reduced data, which would allow to compute more sophisticated photoionization models.
2. The difficulties inherent to an accurate determination of collisional contributions could be avoided by directing the efforts towards the analysis of moderately low-metallicity H II regions.

We would like to acknowledge the referee, Grazyna Stasińska, for a careful reading of the paper and many useful comments. We also thank Yuri Izotov for several constructive suggestions, Gary Ferland for repeated help with Cloudy, and Javier Ballesteros-Paredes and Guillermo Tenorio-Tagle for prompt and detailed explanations. This project has been partially supported by the AYA 3939-C03-01 program. VL is supported by a Marie Curie Fellowship of the European Community programme “*Improving Human Research Potential and the Socio-economic Knowledge Base*” under contract number HPMF-CT-2000-00949. MP’s work was supported in part by grant IN 114601 from DGAPA UNAM.

REFERENCES

- Anderson, H., Ballance, C.P., Badnell, N.R., & Summers, H.P., 2000, *J. Phys. B*, 33, 1255
- Anderson, H., Ballance, C.P., Badnell, N.R., & Summers, H.P., 2002, *J. Phys. B*, 35, 1613
- Baldwin, J. A., Ferland, G. J., Martin, P. G., Corbin, M. R., Cota, S. A., Peterson, B. M., & Slettebak, A. 1991, *ApJ*, 374, 580
- Benjamin, R. A., Skillman, E. D., & Smits, D. P. 1999, *ApJ*, 514, 307
- Benjamin, R. A., Skillman, E. D., & Smits, D. P. 2002, *ApJ*, 569, 288
- Brocklehurst, M. 1971, *MNRAS*, 153, 471
- Brown, T. M., Heap, S. R., Hubeny, I., Lanz, T., & Lindler, D. 2002, *ApJ*, 579, L75
- Burstein, D. & Heiles, C. 1982, *AJ*, 87, 1165
- Cannon, J. M., Skillman, E. D., Garnett, D. R., & Dufour, R. J. 2002, *ApJ*, 565, 931
- Cerviño, M., Luridiana, V., Pérez, E., Vílchez, J. M., and Valls-Gabaud, D. 2003, *A&A* (submitted)

- Cerviño, M., Mas-Hesse, J. M., & Kunth, D. 2002, *A&A*, 392, 19
- Cerviño, M., Valls-Gabaud, D., Luridiana, V., & Mas-Hesse, J. M. 2002, *A&A*, 381, 51
- David, L. P., Jones, C., & Forman, W. 1992, *ApJ*, 388, 82
- Davidson, K. & Kinman, T. D. 1985, *ApJS*, 58, 321
- de Vaucouleurs, G., de Vaucouleurs, A., Corwin, H. G., Buta, R. J., Paturel, G., & Fouqué, P. 1991, Volume 1-3, XII (Springer-Verlag Berlin – Heidelberg – New York)
- Dopita, M. A. & Sutherland, R. S. 2000, *ApJ*, 539, 742
- Ferland, G. J. 2000a, *ASP Conf. Ser.* 216: ADASS IX, 9, 32
- Ferland, G. J. 2000b, *RevMexAA Conf. Series*, 9, 153
- Ferland, G. J. & Osterbrock, D. E. 1985, *ApJ*, 289, 105
- Garnett, D. R., Skillman, E. D., Dufour, R. J., Peimbert, M., Torres-Peimbert, S., Terlevich, R., Terlevich, E., & Shields, G. A. 1995, *ApJ*, 443, 64
- Garnett, D. R., Skillman, E. D., Dufour, R. J., & Shields, G. A. 1997, *ApJ*, 481, 174
- González Delgado, R. M., Leitherer, C., & Heckman, T. M. 1999, *ApJS*, 125, 489
- Izotov, Y. I., Chaffee, F. H., Foltz, C. B., Green, R. F., Guseva, N. G., & Thuan, T. X. 1999, *ApJ*, 527, 757
- Izotov, Y. I., Chaffee, F. H., & Schaerer, D. 2001, *A&A*, 378, L45
- Izotov, Y. I., Foltz, C. B., Green, R. F., Guseva, N. G., & Thuan, T. X. 1997, *ApJ*, 487, L37
- Izotov, Y. I., Lipovetsky, V. A., Chaffee, F. H., Foltz, C. B., Guseva, N. G., & Kniazev, A. Y. 1997, *ApJ*, 476, 698
- Izotov, Y. I. & Thuan, T. X. 1998, *ApJ*, 497, 227
- Izotov, Y. I., Thuan, T. X., & Lipovetsky, V. A. 1997, *ApJS*, 108, 1
- Kingdon, J., & Ferland, G. 1995, *ApJ*, 442, 714
- Kurucz, R. L. 1991, in *Stellar Atmospheres, Beyond Classical Limits*, Crivellari L., Hubeny I., Hummer D.G. (eds.), Kluwer, Dordrecht, p. 441 (<http://kurucz.harvard.edu/grids/>)

- Legrand, F., Kunth, D., Roy, J.-R., Mas-Hesse, J. M., & Walsh, J. R. 1997, *A&A*, 326, L17
- Leitherer, C. et al. 1999, *ApJS*, 123, 3
- Luridiana, V. 2003, proceedings of the XXXVIIth Moriond Astrophysics Meeting “The Cosmological Model” (in press: astro-ph/0209177)
- Luridiana, V., Cerviño, M., & Binette, L. 2001, *A&A*, 379, 1017
- Luridiana, V. & Peimbert, M. 2001, *ApJ*, 553, 633
- Luridiana, V., Peimbert, M., & Leitherer, C. 1999, *ApJ*, 527, 110
- Mas-Hesse, J. M., Cerviño, M., Rodríguez-Pascual, P. M., & Boller, T. 1996, *A&A*, 309, 431
- Mas-Hesse, J. M. & Kunth, D. 1999, *A&A*, 349, 765
- Meynet, G., Maeder, A., Schaller, G., Schaerer, D., & Charbonnel, C. 1994, *A&AS*, 103, 97
- Oey, M. S., Dopita, M. A., Shields, J. C., & Smith, R. C. 2000, *ApJS*, 128, 511
- Osterbrock, D. E. 1989, *Astrophysics of gaseous nebulae and active galactic nuclei* (Mill Valley: University Science Books)
- Pagel, B. E. J., Edmunds, M. G., Blackwell, D. E., Chun, M. S., & Smith, G. 1979, *MNRAS*, 189, 95
- Peimbert, A. 2003, *ApJ*, 584, 735
- Peimbert, A., Peimbert, M., & Luridiana, V. 2002, *ApJ*, 565, 668 (Paper I)
- Peimbert, M. 1967, *ApJ*, 150, 825
- Peimbert, M., Peimbert, A., Luridiana, V., & Ruiz, M. T. 2003, in “Star Formation through Time”, Pérez, E., González Delgado, R., & Tenorio-Tagle, G. (eds.), *ASP Conference Series* (in press: astro-ph/0211497)
- Peimbert, M., Peimbert, A., & Ruiz, M. T. 2000, *ApJ*, 541, 688
- Relaño, M., Peimbert, M., & Beckman, J. 2002, *ApJ*, 564, 704
- Sawey, P. M. J., & Berrington, K. A., 1993, *Atomic Data and Nuclear Data Tables*, 55, 81
- Schaerer, D., de Koter A. 1997, *A&A*, 322, 598
- Schaller, G., Schaerer, D., Meynet, G., & Maeder, A. 1992, *A&AS*, 96, 269

- Schlegel, D. J., Finkbeiner, D. P., & Davis, M. 1998, *ApJ*, 500, 525
- Schmutz, W., Leitherer, C., & Gruenwald, R. 1992, *PASP*, 104, 1164
- Skillman, E. D. & Kennicutt, R. C. 1993, *ApJ*, 411, 655
- Smith, L. J., Norris, R. P. F., & Crowther, P. A. 2002, *MNRAS*, 337, 1309
- Smits, D. P. 1996, *MNRAS*, 278, 683
- Stasińska, G. 1990, *A&AS*, 83, 501
- Stasińska, G. & Izotov, Y. I. 2001, *A&A*, 378, 817
- Stasińska, G. & Schaerer, D. 1999, *A&A*, 351, 72
- Stasińska, G. & Szczerba, R. 2001, *A&A*, 379, 1024
- Stevens, I. R. & Strickland, D. K. 1998, *MNRAS*, 301, 215
- Storey, P. J., & Hummer, D. G. 1995, *MNRAS*, 272, 41
- Thuan, T. X., Izotov, Y. I., & Lipovetsky, V. A. 1997, *ApJ*, 477, 661
- Torres-Peimbert, S., Peimbert, M., & Fierro, J. 1989, *ApJ*, 345, 186
- Viallefond, F. & Thuan, T. X. 1983, *ApJ*, 269, 444
- Viegas, S. 2003, *Star Formation through Time*, *PASP*, Conference Series (in press)
- Vílchez, J. M. & Iglesias-Páramo, J. 1998, *ApJ*, 508, 248
- Zurita, A., Rozas, M., & Beckman, J. E. 2001, *Ap&SS*, 276, 1015

Table 1. Comparison between some observed and predicted quantities for SBS 0335–052^a

Quantity	Center		0".6		Complete slit		Complete model
	Observed	Predicted	Observed	Predicted	Observed	Predicted	Predicted
[O II] λ 3727/H β	0.253	0.187	0.256	0.268	0.279	0.259	0.319
[O III] λ 4363/H β	0.113	0.098	0.115	0.079	0.115	0.083	0.075
He II λ 4686/H β	0.031	0.001	0.032	0.001	0.032	0.001	0.001
[O III] λ 5007/H β	3.273	3.388	3.282	2.972	3.202	3.055	2.871
[O I] λ 6300/H β	0.006	0.003	0.006	0.004	0.006	0.004	0.005
[S II] λ 6725/H β	0.035	0.027	0.036	0.039	0.039	0.035	0.046
[O II] λ 7325/H β	...	0.010	...	0.014	...	0.013	0.014
[S II] 6716/6731	1.071	1.023	1.063	1.064	1.121	1.084	1.175
$T(\text{O II})$	15800	15500	15950	15250	15950	15250	15050
$T(\text{O III})$	20400	18350	20850	17550	20950	17750	17400
R^b	1000	1300	1000	1300	1000	1300	1300
Log $L(\text{H}\beta)^c$	40.08	40.12	39.91	39.89	40.61	40.61	41.04

^aComparison between some observed quantities for SBS 0335–052 and the corresponding quantities predicted according to the multiple-shell model A, with the aperture effect included. The H β intensity includes the collisional contribution. The observed [O III] temperatures, $T(\text{O III})$, are computed from the line intensities reported by Izotov et al. 1999; the observed [O II] temperatures, $T(\text{O II})$, have been obtained from $T(\text{O III})$ with the analytical fit of Izotov et al. 1999 to the models of Stasińska 1990. The predicted $T(\text{O II})$ and $T(\text{O III})$ values have been obtained as described in Section 2.3.

^bIn parsecs.

^cIn erg s^{-1} .

Table 2. Miscellaneous predicted quantities for the multiple-shell model A of SBS 0335–052^a

Quantity	Center	0".6	Complete slit	Complete model
T_0	17950	17150	17300	17000
T_{02}	14900	14750	14750	14550
$T(\text{O II})$	15500	15250	15250	15050
T_{03}	18150	17350	17550	17250
$T(\text{O III})$	18350	17550	17750	17400
t^2	0.007	0.007	0.008	0.008
t_2^2	0.023	0.020	0.020	0.019
t_3^2	0.005	0.004	0.005	0.005
O^+/O	0.061	0.092	0.087	0.108
$icf(\text{He})$	0.993	0.990	0.991	0.988

^aThis model has the following properties: Salpeter’s IMF with Monte Carlo sampling; $M_{up} = 120 M_\odot$; continuous star-formation law; age $t = 3.0$ Myr; standard mass-loss rate; $Z_* = 0.001$; $Z_{gas} = 0.0007$. See Section 3.2.3 for further details.

Table 3. Collisional contribution to the total Balmer intensities for the three multiple-shell models of SBS 0335–052.

Quantity	Model A			Model B			Model C		
	Center	0''.6	Slit	Center	0''.6	Slit	Center	0''.6	Slit
$I(\text{H}\alpha)_{\text{col}}/I(\text{H}\alpha)_{\text{tot}}$	0.069	0.078	0.074	0.113	0.117	0.117	0.233	0.272	0.280
$I(\text{H}\beta)_{\text{col}}/I(\text{H}\beta)_{\text{tot}}$	0.020	0.022	0.021	0.035	0.036	0.035	0.071	0.082	0.084
T_{03}	18150	17350	17550	20900	19200	19100	20870 ^a	19860 ^a	20090 ^a
$C(\text{H}\beta)^{\text{col}}$	0.07	0.08	0.07	0.11	0.11	0.12	0.25	0.30	0.31

^aThese temperatures are fictitious and have been obtained by multiplying by 1.15 the corresponding temperatures in model A (see Section 3.3).

Table 4. Comparison between some observed and predicted quantities for I Zw 18^a

Quantity	Slit		Complete model
	Observed	Predicted	Predicted
[O II] λ 3727/H β	0.502	0.202	0.255
[O III] λ 4363/H β	0.054	0.051	0.044
He II λ 4686/H β	0.009	0.001	0.001
[O III] λ 5007/H β	1.749	1.668	1.496
[O I] λ 6300/H β	0.012	0.003	0.004
[S II] λ 6725/H β	0.069	0.031	0.041
[O II] λ 7325/H β	...	0.006	0.008
[S II] 6716/6731	1.477	1.390	1.393
$T(\text{O II})$	15400	15150	14700
$T(\text{O III})$	19060	18950	18650
R^b	40 – 100	78	78
Log $L(\text{H}\beta)^c$	38.32	38.32	...
Log $L(\text{H}\beta)^d$	38.49	...	38.43

^aComparison between the observed line intensities relative to H β for the SE knot of I Zw 18 and the predictions of model A, with the aperture effect included. The slit size is $1.5'' \times 3.5''$. The H β intensity includes the collisional contribution. The observed $T(\text{O II})$ and $T(\text{O III})$ are those reported by Izotov et al. 1999. The predicted $T(\text{O II})$ and $T(\text{O III})$ values have been obtained as described in Section 2.3.

^bIn parsecs.

^cIn erg s^{-1} ; observed with a $1.5'' \times 3.5''$ slit (Izotov et al. 1999).

^dIn erg s^{-1} ; observed in the complete region (Cannon et al. 2002).

Table 5. Miscellaneous predicted quantities for models A and B of I Zw 18.

Quantity	Model A ^a	Model B ^a
T_0	18200	19600
T_{02}	14650	14950
$T(\text{O II})$	15150	15700
T_{03}	18700	20250
$T(\text{O III})$	18950	21200
t^2	0.018	0.032
t_2^2	0.022	0.030
t_3^2	0.012	0.023
O^+/O	0.118	0.119
$icf(\text{He})$	0.991	0.991

^aAs seen through a slit of $1.5'' \times 3.5''$.

Table 6. Collisional contribution to the total Balmer intensities in I Zw 18.

Quantity	Model A ^a	Model B ^a
$I(\text{H}\alpha)_{\text{col}}/I(\text{H}\alpha)_{\text{tot}}$	0.060	0.080
$I(\text{H}\beta)_{\text{col}}/I(\text{H}\beta)_{\text{tot}}$	0.017	0.024
T_{03}	18700	20250
$C(\text{H}\beta)^{\text{col}}$	0.06	0.08

^aAs seen through a slit of $1.5'' \times 3.5''$.

Table 7. Comparison between some observed and predicted quantities of object H 29^a

Quantity	Observed	Predicted
[O II] λ 3727/H β	0.719	0.522
[O III] λ 4363/H β	0.127	0.097
He II λ 4686/H β	0.012	0.001
[O III] λ 5007/H β	5.543	5.203
[O I] λ 6300/H β	0.014	0.009
[S II] λ 6725/H β	0.106	0.085
[O II] λ 7325/H β	...	0.015
[S II] 6716/6731	1.356	1.377
$T(\text{O II})^b$	14000	13950
$T(\text{O III})^b$	15400	14750
R^c	$\gtrsim 30$	55
$\text{Log } L(\text{H}\beta)^d$	38.72	38.70

^aNo aperture effect included. The H β intensity includes the collisional contribution.

^bBoth the observed $T(\text{O II})$ and $T(\text{O III})$ are those reported by Izotov et al. 1997. The predicted $T(\text{O II})$ and $T(\text{O III})$ values have been obtained as described in Section 2.3.

^cIn parsecs.

^dIn erg s^{-1} .

Table 8. Miscellaneous predicted quantities for H 29.

Quantity	Model A ^a
T_0	14650
T_{02}	13700
$T(\text{O II})$	13950
T_{03}	14750
$T(\text{O III})$	14750
t^2	0.001
t_2^2	0.009
t_3^2	<0.001
O^+/O	0.086
$icf(\text{He})$	0.991

^aNo aperture correction applied.

Table 9. Collisional contribution to the total Balmer intensities in H 29.

Quantity	Model A ^a
$I(\text{H}\alpha)_{\text{col}}/I(\text{H}\alpha)_{\text{tot}}$	0.028
$I(\text{H}\beta)_{\text{col}}/I(\text{H}\beta)_{\text{tot}}$	0.007
T_{03}	13700
$C(\text{H}\beta)^{\text{col}}$	0.03

^aNo aperture correction applied.

Table 10. Observed, collisional, and collision-corrected reddening coefficients for SBS 0335–052, I Zw 18, and H 29.

Quantity	SBS 0335–052			I Zw 18	H 29
	Center	0".6	Complete slit	Complete slit	Complete model
$C(\text{H}\beta)^{\text{obs}}$	0.23±0.02	0.25±0.02	0.26±0.02	0.10±0.02	0.07±0.08
$C(\text{H}\beta)^{\text{col}}$	0.11±0.04	0.11±0.03	0.12±0.05	0.06±0.02	0.03±0.02
$C(\text{H}\beta)^{\text{true}}$	0.12±0.04	0.14±0.04	0.14±0.06	0.04±0.02	0.04±0.05

Table 11. Helium abundance in SBS 0335–052.

λ	$\frac{F(\lambda)}{F(\text{H}\beta)}$ ^a	$\frac{I(\lambda)}{I_{\text{tot}}(\text{H}\beta)}$ ^b	$\frac{I(\lambda)}{I_{\text{rec}}(\text{H}\beta)}$ ^c	$\frac{I(\lambda)}{I_{\text{rec}}(\text{H}\beta)}$ ^d
3889 ^e	0.1606 ± 0.0018	0.1997	0.2069	0.1958
4026	0.0122 ± 0.0005	0.0173	0.0179	0.0171
4471	0.0340 ± 0.0006	0.0382	0.0396	0.0387
4686	0.0292 ± 0.0006	0.0303	0.0314	0.0310
4922	0.0077 ± 0.0005	0.0093	0.0096	0.0097
5876	0.1167 ± 0.0014	0.1027	0.1064	0.1126
6678	0.0322 ± 0.0006	0.0263	0.0273	0.0297
7065	0.0425 ± 0.0006	0.0358	0.0371	0.0409
$C(\text{H}\beta)$...	0.24 ± 0.02	0.24 ± 0.02	0.13 ± 0.04
$\langle y^+ \rangle$...	0.07635	0.07860	0.08099
$\langle y^{++} \rangle$...	0.00269	0.00279	0.00275
Y	...	0.2384 ± 0.0048	0.2438 ± 0.0050	0.2491 ± 0.0055

^aFlux observed in the three centermost extractions of the slit used by Izotov et al. 1999, corrected for underlying absorption (see Paper I).

^bReddening-corrected flux, neglecting the collisional contribution.

^cReddening-corrected flux, with the collisional contribution subtracted from $F(\text{H}\beta)$ but not from the reddening coefficient.

^dReddening-corrected flux, with the collisional contribution subtracted from both $F(\text{H}\beta)$ and the reddening coefficient.

^eSum of He I 3889 + H8; the value of $I(\text{H8})/I(\text{H}\beta)$ is 0.1073.

Table 12. Helium abundance in I Zw 18.

λ	$\frac{F(\lambda)}{F(\text{H}\beta)}$ ^a	$\frac{I(\lambda)}{I_{\text{tot}}(\text{H}\beta)}$ ^b	$\frac{I(\lambda)}{I_{\text{rec}}(\text{H}\beta)}$ ^c	$\frac{I(\lambda)}{I_{\text{rec}}(\text{H}\beta)}$ ^d
3889 ^e	0.1570 ± 0.0043	0.2057	0.2093	0.1931
4026	0.0151 ± 0.0036	0.0210	0.0214	0.0208
4471	0.0352 ± 0.0025	0.0394	0.0401	0.0396
4686	0.0089 ± 0.0023	0.0090	0.0091	0.0091
5876	0.0968 ± 0.0028	0.0898	0.0914	0.0941
6678	0.0273 ± 0.0019	0.0246	0.0250	0.0262
7065	0.0249 ± 0.0016	0.0222	0.0226	0.0238
$C(\text{H}\beta)$...	0.10 ± 0.02	0.10 ± 0.02	0.04 ± 0.02
$\langle y^+ \rangle$...	0.07552	0.07701	0.07728
$\langle y^{++} \rangle$...	0.00081	0.00082	0.00082
Y	...	0.2338 ± 0.0072	0.2373 ± 0.0073	0.2379 ± 0.0073

^aObserved flux by Izotov et al. 1999, corrected for underlying absorption (see Paper I).

^bReddening-corrected flux, neglecting the collisional contribution.

^cReddening-corrected flux, with the collisional contribution subtracted from $F(\text{H}\beta)$ but not from the reddening coefficient.

^dReddening-corrected flux, with the collisional contribution subtracted from both $F(\text{H}\beta)$ and the reddening coefficient.

^eSum of He I 3889 + H8; the value of $I(\text{H8})/I(\text{H}\beta)$ is 0.1073.

Table 13. Helium abundance in H 29.

λ	$\frac{F(\lambda)}{F(\text{H}\beta)}$ ^a	$\frac{I(\lambda)}{I_{\text{tot}}(\text{H}\beta)}$ ^b	$\frac{I(\lambda)}{I_{\text{rec}}(\text{H}\beta)}$ ^c	$\frac{I(\lambda)}{I_{\text{rec}}(\text{H}\beta)}$ ^d
3820	0.007 ± 0.001	0.010	0.010	0.010
3889 ^e	0.186 ± 0.001	0.208	0.210	0.207
4026	0.016 ± 0.001	0.021	0.021	0.020
4387	0.004 ± 0.001	0.005	0.005	0.005
4471	0.037 ± 0.001	0.039	0.040	0.040
4686	0.012 ± 0.001	0.012	0.012	0.012
4922	0.009 ± 0.001	0.011	0.011	0.011
5876	0.103 ± 0.001	0.098	0.099	0.101
6678	0.029 ± 0.001	0.027	0.028	0.028
7065	0.025 ± 0.001	0.023	0.023	0.023
7281	0.005 ± 0.001	0.005	0.005	0.005
$C(\text{H}\beta)$...	0.07 ± 0.08	0.07 ± 0.08	0.04 ± 0.05
$\langle y^+ \rangle$...	0.07776	0.07836	0.07882
$\langle y^{++} \rangle$...	0.00104	0.00104	0.00104
Y	...	0.2375 ± 0.0040	0.2389 ± 0.0040	0.2400 ± 0.0041

^aObserved flux by Izotov et al. 1997, corrected for underlying absorption (see Paper I).

^bReddening-corrected flux, neglecting the collisional contribution.

^cReddening-corrected flux, with the collisional contribution subtracted from $F(\text{H}\beta)$ but not from the reddening coefficient.

^dReddening-corrected flux, with the collisional contribution subtracted from both $F(\text{H}\beta)$ and the reddening coefficient.

^eSum of He I 3889 + H8; the value of $I(\text{H8})/I(\text{H}\beta)$ is 0.106.

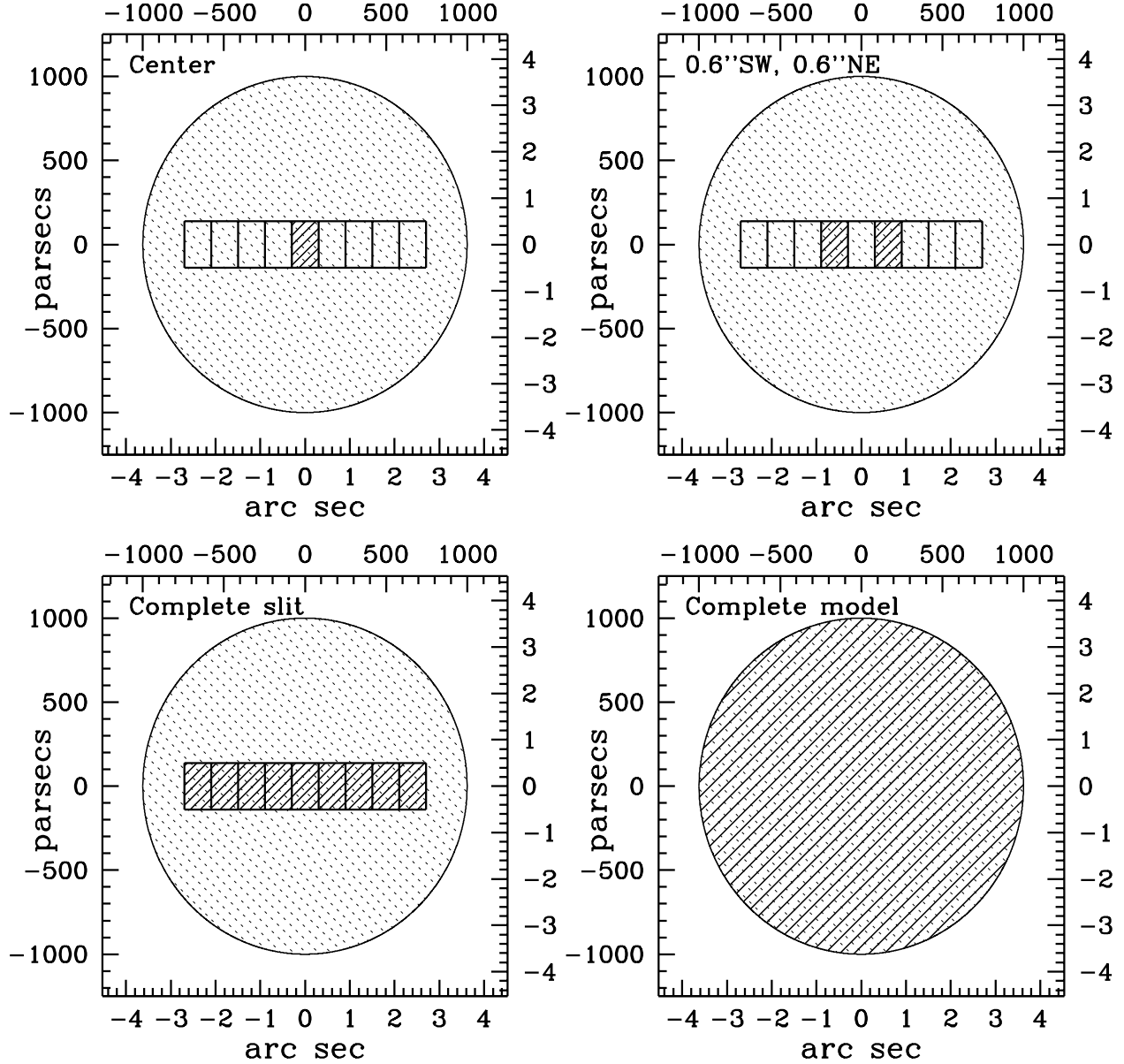


Fig. 1.— Sketch of the slit used by Izotov et al. (1999) and the nine extractions making it up, projected onto the model nebula. This figure also provides a visual explanation for the meaning of the column headers of Tables 1 and 2. The left and lower axes of each panel are in arc sec, the right and upper axes are in parsecs and assume a distance $d = 57$ Mpc (see Sections 2.3, 3.1, and 3.2.3).

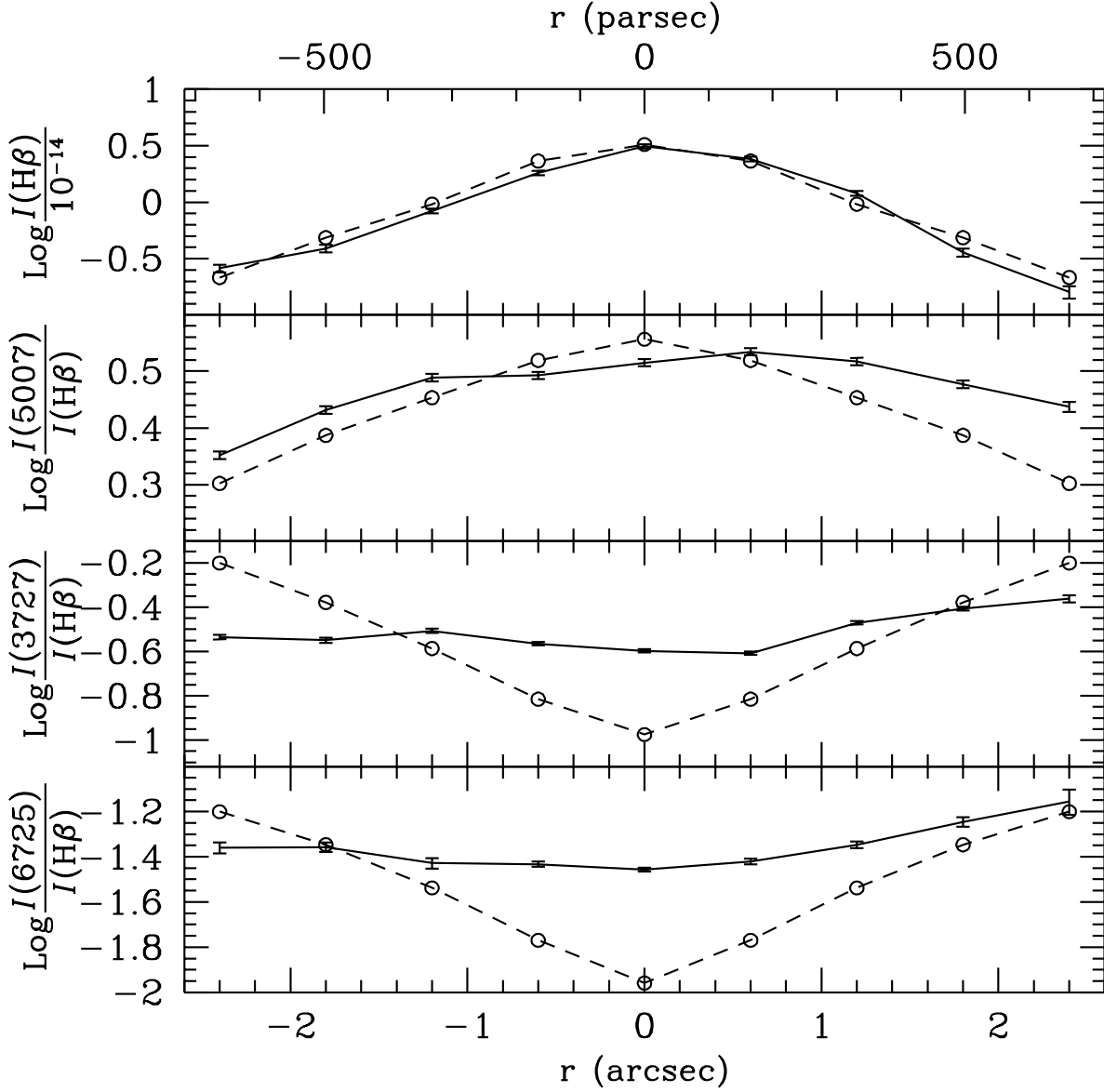


Fig. 2.— Line profiles for the Gaussian model of SBS 0335–052. Solid lines: observations, dashed line: model. The $H\beta$ intensity is in $\text{erg s}^{-1} \text{cm}^{-2}$.

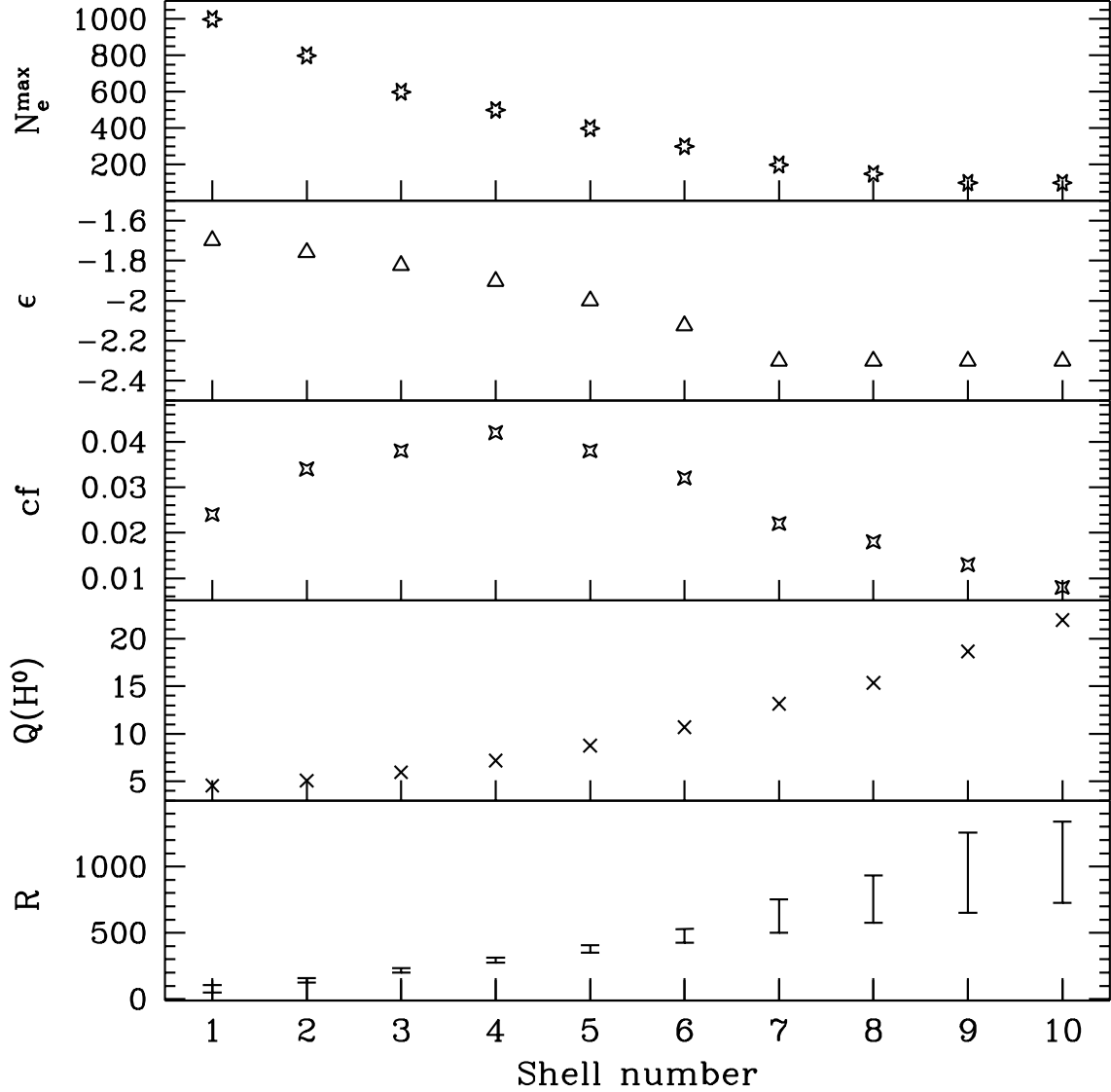


Fig. 3.— Input parameters of the ten shells that compose the multiple-shell model A. The density law in each shell is given by $N_e = \max(N_e^{\max} \exp(r/r_0)^{-2}, N_e^{\min})$, with $r_0 = 260$ pc, $N_e^{\min} = 90 \text{ cm}^{-3}$ equal in all the the shells, and N_e^{\max} given by the values plotted in the upper panel. The second panel from the top gives the filling factor values of each shell; the third panel from the top gives the covering factor values; the effective covering factor, averaging $\langle cf \rangle = 0.22$ over the model. The fourth panel from the top gives the rate of ionizing photons emitted, in units 10^{53} s^{-1} ; finally, the bottom panel shows the radius range spanned by each shell, in parsecs.

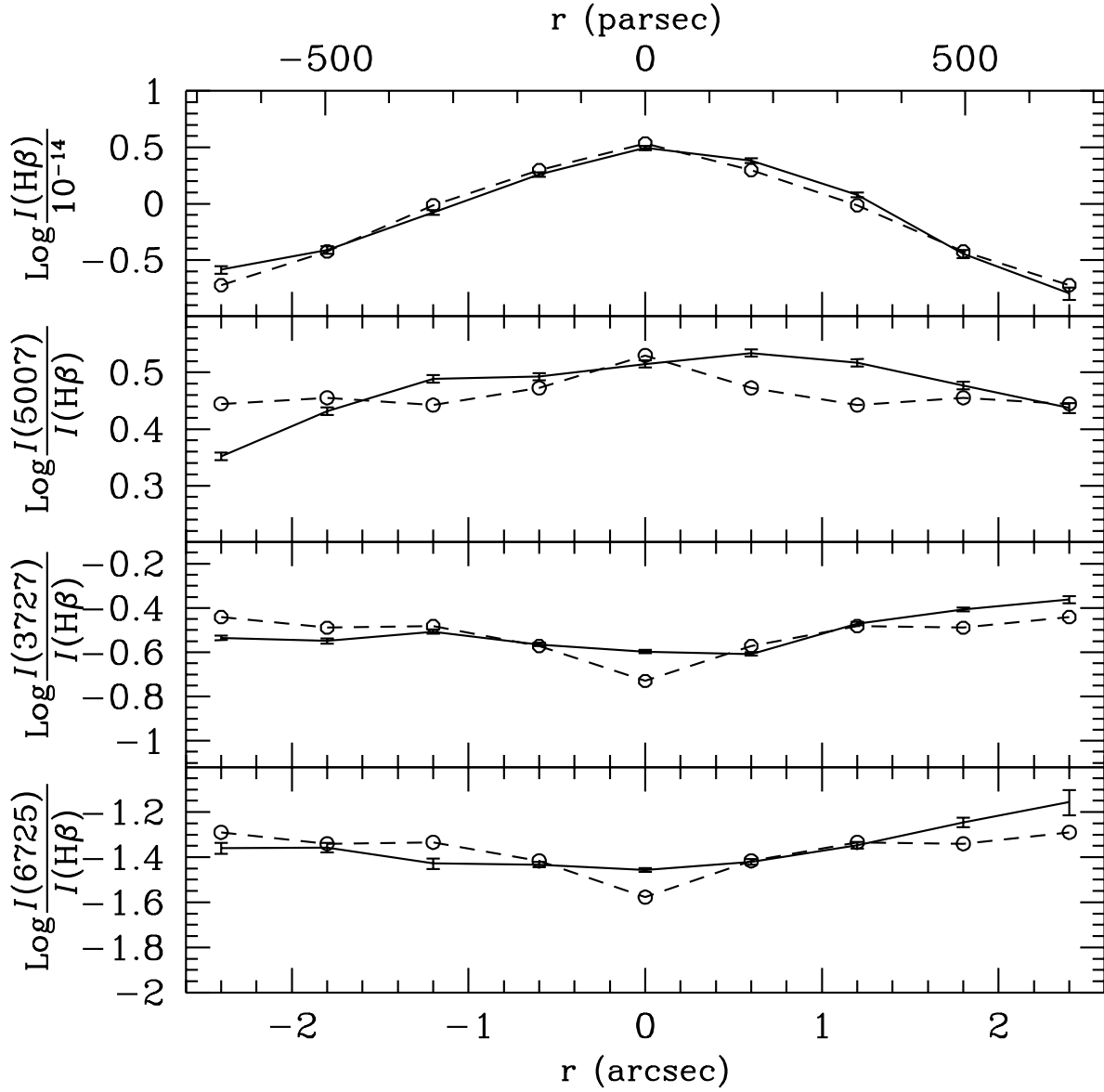


Fig. 4.— Line profiles for the best multiple-shell model A of SBS 0335–052. Solid lines: observations, dashed line: model. The H β intensity is in $\text{erg s}^{-1} \text{cm}^{-2}$.

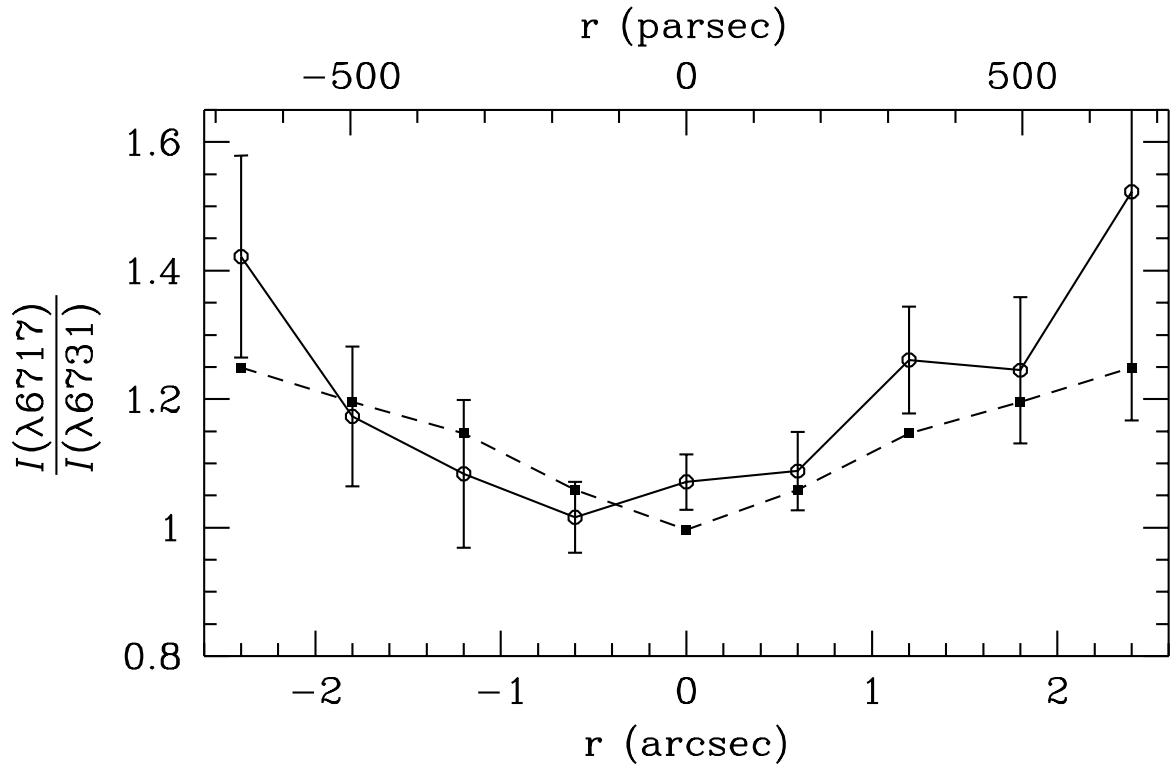


Fig. 5.— Comparison between the observed [S II] 6716/6731 ratio profile (solid line) and the corresponding predicted values (dashed line) for the multiple-shell model A of SBS 0335–052.

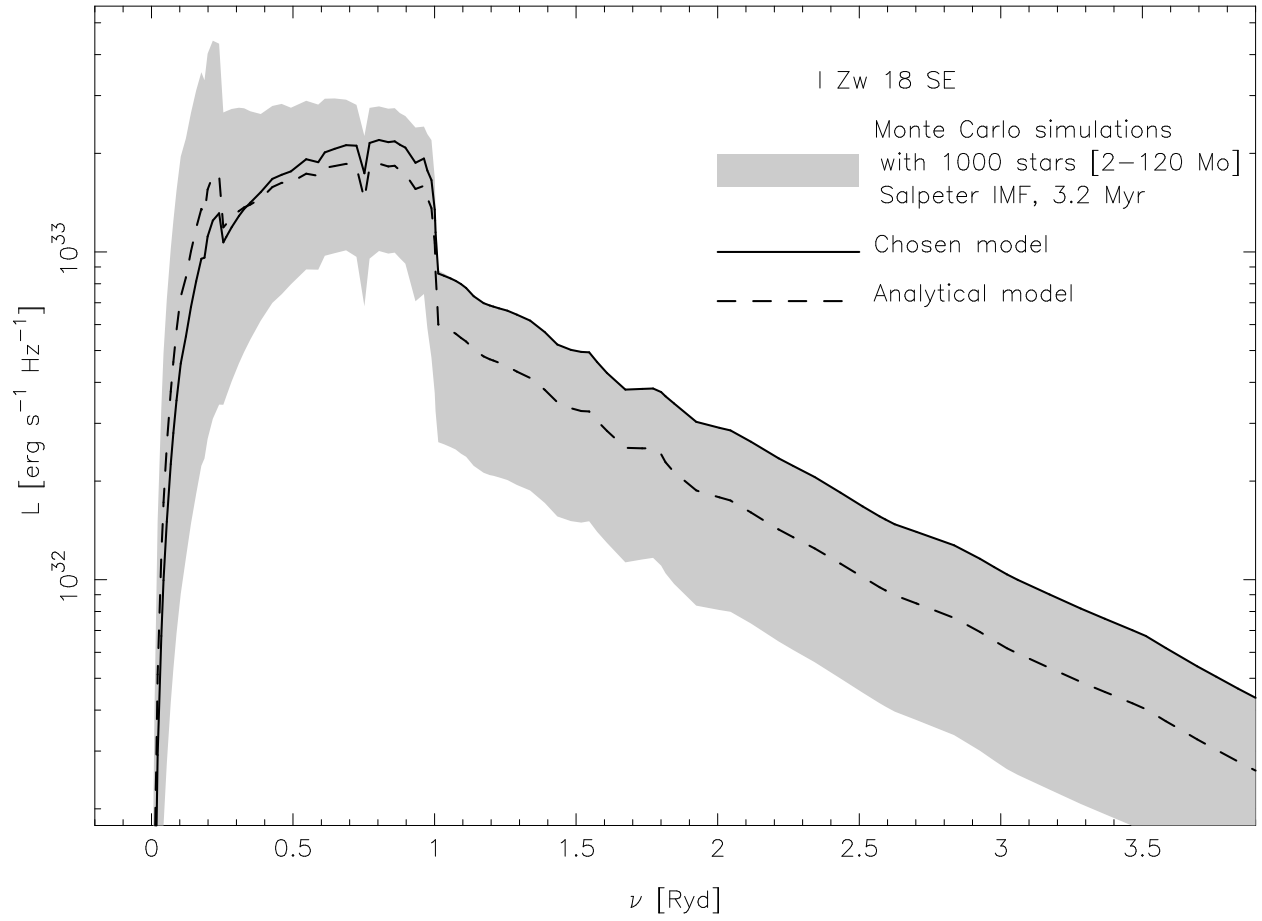


Fig. 6.— Comparison between the analytical (dashed line) and the Monte Carlo spectra (shaded region) of I Zw 18. The selected spectrum is shown as a solid line.

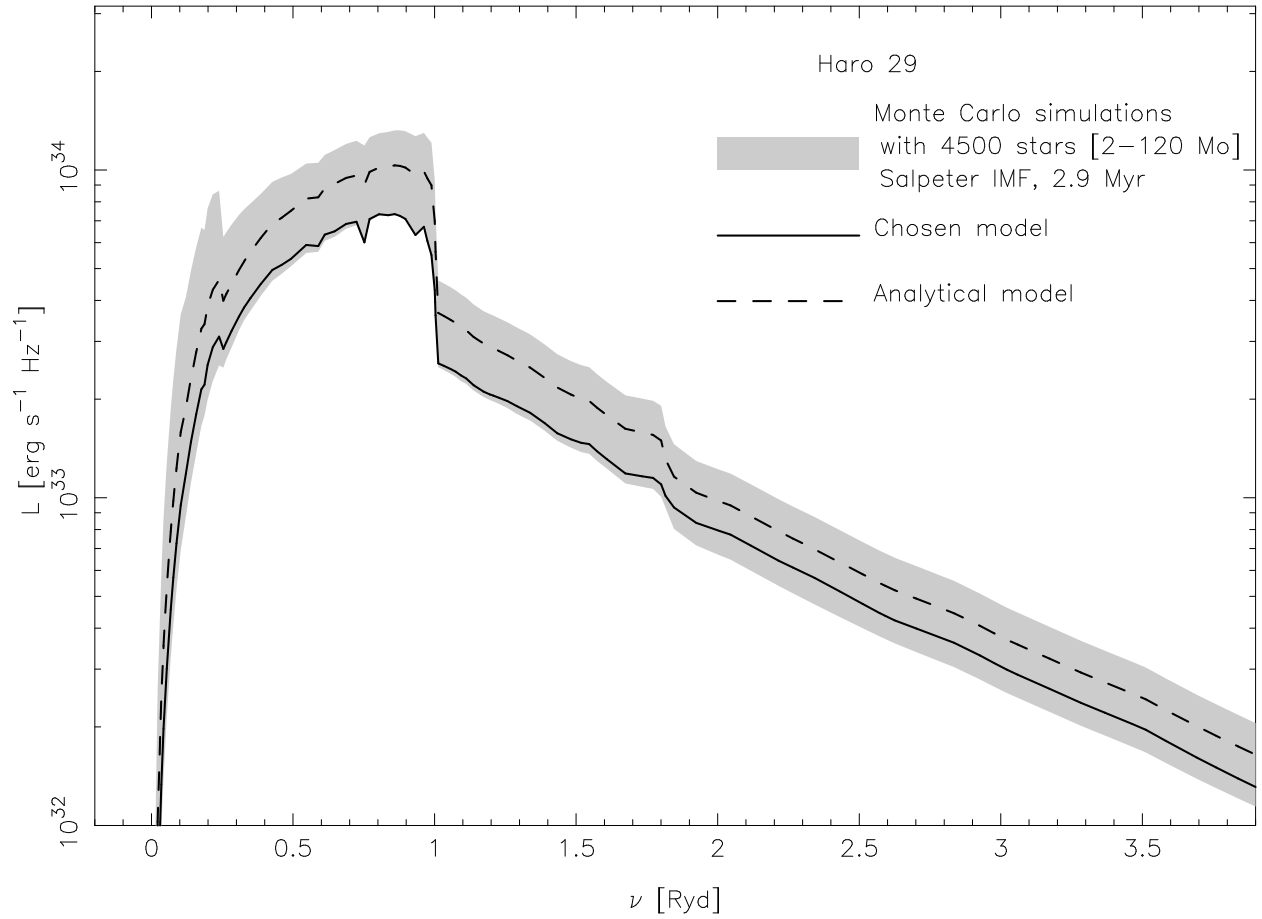


Fig. 7.— Comparison between the analytical (dashed line) and the Monte Carlo spectra (shaded region) of H 29. The selected spectrum is shown as a solid line.

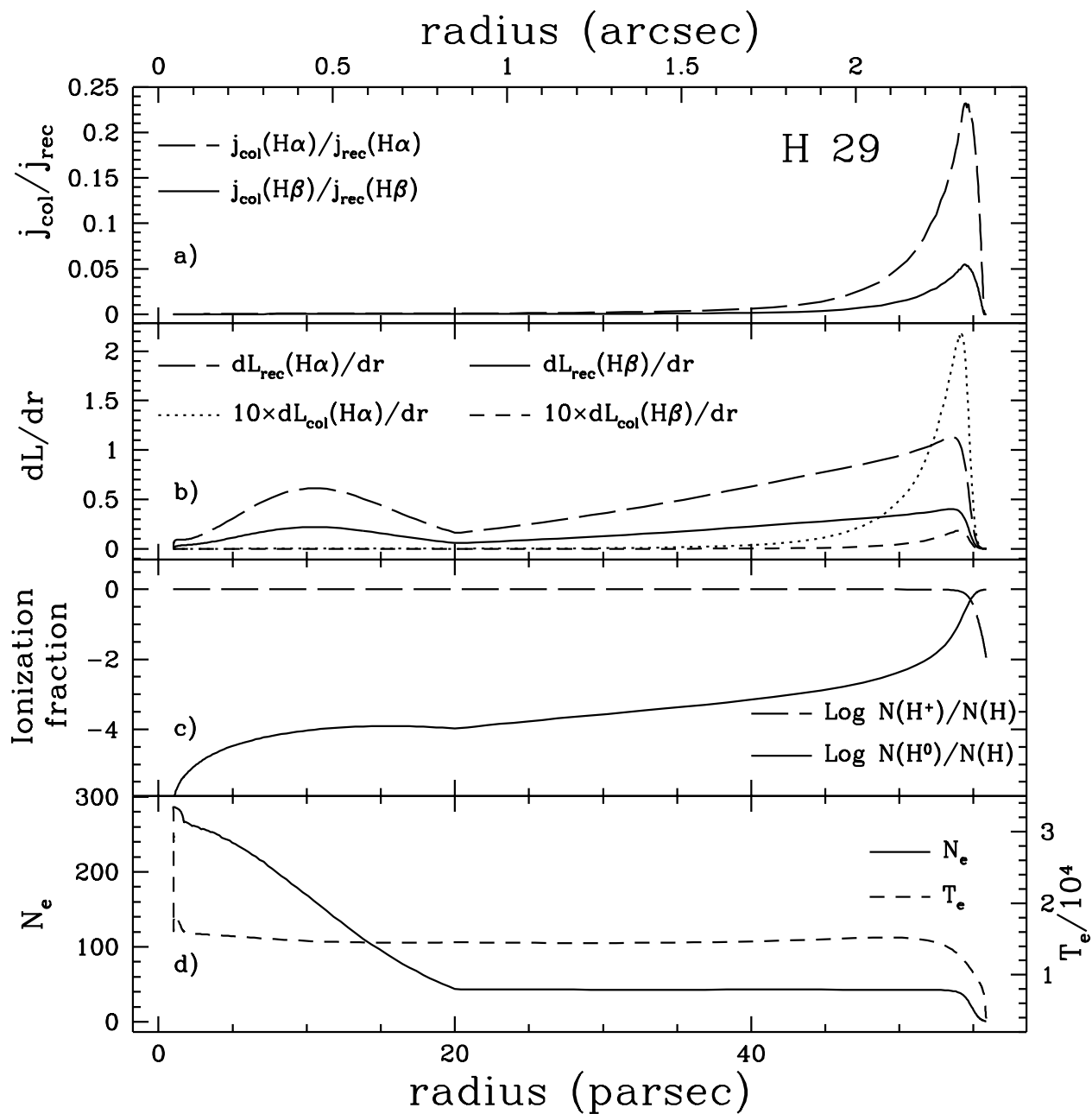


Fig. 8.— Some predicted quantities for model A of H 29. Panel a): radial behavior of the ratio between the collisional and the recombination emissivities of H α and H β . Panel b): incremental contribution of each shell to the total luminosities, with the volume factor taken into account; units are 10^{38} erg sec $^{-1}$ pc $^{-1}$. Panel c): radial behavior of the hydrogen ionization fractions. Panel d): radial behavior of the electron temperature and density.